Probing the Dynamics of Shallow Cumulus Convection

Probing the Dynamics of Shallow Cumulus Convection

A dissertation presented

by

Ji Nie

to

The Department of Earth and Planetary Sciences

in partial fulfillment of the requirements
for the degree of

Doctor of Philosophy

in the subject of

Earth and Planetary Sciences

Harvard University
Cambridge, Massachusetts

September 2013

Dissertation Advisor: Professor Zhiming Kuang Ji Nie

Probing the Dynamics of Shallow Cumulus Convection

Abstract

Our limited knowledge of convection and its poor representation in climate models is one of the factors that most hamper our ability to understand and predict the climate system. In this thesis, the dynamics of shallow cumulus convection are probed using Large-eddy simulations (LES) and simple models.

Responses of shallow cumuli to large-scale temperature/moisture perturbations are examined through diagnostics of LES and a stochastic parcel model. The parcel model reproduces most of the changes in the LES-simulated cloudy updraft statistics in response to the perturbations. Analyses of parcel histories show that a positive temperature perturbation forms a buoyancy barrier, which preferentially eliminates parcels that start with lower equivalent potential temperature or have experienced heavy entrainment. Besides the amount of entrainment, the height at which parcels entrain is also important in determining their fate. The stochastic entrainment is key for the parcel model to reproduce the LES results.

We further explore the feasibility of a stochastic-parcel-based cumulus parameterization. In this parameterization, air parcels are released from the surface layer and integrated forward in time until becoming quiescent. During the integration, parcels entrain episodically and stochastically. Temperature/moisture fluxes associated with the parcels are used to calculate convective tendencies. Initial results show that this simple parameterization produces realistic convective tendencies and reproduces the LES-simulated mean and variance of cloudy updraft

properties. The evolution of the introduced temperature/moisture perturbations calculated by the linear response functions of the parameterization also generally matches the results of LES.

To evaluate the representation of mixing in multiple plume/parcel models, for example, the stochastic parcel model, a new framework is proposed, where the vertical evolution of the cloud mass flux distribution as a function of given properties is viewed as a mapping process. Matrices that characterize this mapping process are constructed using a Lagrangian particle dispersion model embedded in a LES. The construction of these mapping matrices from LES provides a reference, against which multiple-parcel models can be compared. The framework is further applied to diagnose the response of shallow cumuli to a small temperature perturbation.

Permissions

Chapter 2 and 3 are substantially based upon:

Nie, J. and Z. Kuang, 2012: Responses of shallow cumulus convection to large-scale temperature and moisture perturbations: a comparison of large-eddy simulations and a convective parameterization based on stochastically entraining parcels, J. Atmos. Sci., 69, 1936-1956.

Chapter 4 is substantially based upon:

Nie, J. and Z. Kuang, 2012: Beyond bulk entrainment and detrainment rates: a new framework for diagnosing mixing in cumulus convection, Geophys. Res. Lett. 39, L21803.

CONTENTS

List of Figures

corresponding to mass flux changes shown in (a)-(d), together with δF_{qt} from the LES. In (e) the δD, δA and δE terms are multiplied by a factor of 3 for better illustration. (f) introduced temperature perturbation.

Figure A1: Cloud updraft statistics of (left) mass flux, (middle) w, and (right) θ_e with different LES settings as listed in Table A1. The simulation names are labeled on the top-left corner of each panel. The panels for the CTL simulations are as in figure 2-2a to c and are included here to facilitate comparison.

List of Tables

List of Acronyms

3D:	3-Dimensional
BOMEX:	Barbados Oceanographic and Meteorological Experiment
CRM:	Cloud Resolving Model
GCM:	Global Climate Model
ITCZ:	Intertropical Convergence Zone
LES:	Large-Eddy Simulation
LPDM:	Lagrangian Particle Dispersion Model
LRF:	Linear Response Function
PDF:	Probability Distribution Function
SPM:	Stochastic Parcel Model
SST:	Sea Surface Temperature

Acknowledgements

As of this moment, it is hard for me to believe that more than five years have been passed since I joined the Department of Earth and Planetary Sciences. During this unique period, I have received help from lots of people in many ways. I shall express my sincere gratitude to them.

First of all, I would like to thank my advisor and mentor Zhiming Kuang for his guidance, encouragement, patience, and generosity throughout the five years. I benefit from his invaluable advices in many aspects.

I would like to thank my committee members, Porf. Eli Tziperman and Prof. Brian Farrell, who watched me and kept me on the track.

Thanks go to the people who create the warm and friendly environment of the department, to the fellow graduate students who are always enthusiastic about discussion, to the past and current members of Zhiming's group, especially Bill Boos and David Romps for the help in research and Mary Moore for improving my writing.

I am deeply grateful to John Osepchuk, Shirley Osepchuk, Lauren Osepchuk, Mark Leighton and many other members in the big families, who invited me to the Christmas and Easter feasts every year and more importantly shared the family warmth with me.

To my parents, I cannot thank you enough for years of selfless love and devotion.

CHAPTER 1

INTRODUCTION

Clouds are one of the atmospheric phenomena that were well perceived even before the dawn of civilization. Our ancestors had started using clouds to predict the weather since thousands of years ago. However, despite many years passed, clouds are still among the most stubborn questions in the atmospheric and climate sciences.

Clouds and convection are important because they play a significant, and sometimes central, role in many climate and atmospheric circulation problems. However, to understand and parameterize clouds are challenging due to the complicated dynamics and the insufficient observations. To atmospheric scientists, clouds and convection are rich and charming areas with many open questions.

In this chapter, I first motivate the study by introducing the importance of clouds in climate. The introduction mostly focuses on shallow and low clouds. Next, I overview the background theories of shallow cumulus convection as well as recent advances in this area. Different groups of simple cloud models are compared with each other, and discussions are put in the context of how the models treat the key processes of convection: the entrainment and detrainment mixing. Finally, I introduce the numerical models and tools that are used extensively in this thesis, followed by the outline of the thesis.

1.1 Low clouds and climate

The clouds feed back on climate mainly through changing the radiative flux. On the one hand, by reflecting shortwave radiation, the presence of clouds increases the planetary albedo and cools the surface. On the other hand, as a very efficient longwave absorption agent, clouds can trap the longwave in the atmosphere and warm the surface. The net radiative forcing of a cloud can either be positive or negative, depending on the detailed properties of the cloud such as cloud top height, cloud brightness, and so on. Low clouds have strong negative net radiative forcing, because the longwave warming is relative weak and does not cancel much of the cooling caused by the reflection of solar insolation.

Shallow cumulus convection also plays an important role in the large-scale tropical atmospheric circulation. It has long been recognized that representations of shallow cumulus convection in GCMs (General Circulation Model/Global Climate Models) significantly impact the resulting circulation (e.g. Tiedtke 1989). By enhancing vertical transport of heat and moisture, shallow cumuli regulate the surface fluxes and maintain the thermodynamic structures over the vast subtropical trade wind region; a region that also provides the inflow for the deep convective intertropical convergence zone (ITCZ). Through this mechanism chain, shallow cumulus convection can feed back on the deep convective activity in the ITCZ and the strength of the Hadley circulation (e.g. Neggers *et al.* 2007).

More recently, it is further suggested that, because of the abundance, the shallow cloud is a leading factor in determining the cloud-climate feedback (Bony *et al.* 2004, Bony and Dufresne 2005). On average, about one fifth of the global area is covered with shallow clouds (Wood 2012); thus only a small percentage change of the shallow cloud amount can lead to a climate forcing as large as the forcing by anthropic CO_2 emmision (Randall et al. 1984, Slingo 1990). In

GCM doubling CO_2 simulations, it is found that the uncertainty of cloud feedback, which has the largest uncertainty compared with other climate feedbacks (e.g. Dufresne and Bony 2008), is mostly due to the uncertainty of low cloud coverage changes (Zelinka *et al.* 2013). The intermodel differences of low cloud feedback contribute to about 75% of the intermodel differences in cloud feedback (Soden and Vecchi 2011, Zelinka *et al.* 2013). Under global warming, the changes of low cloud coverage may be due to the changes of middle troposphere subsidence (e.g. Lu et al. 2007, Vecchi and Soden 2007) or boundary layer adjustment processes (e.g. Rieck *et al.* 2012).

1.2 Simple models of shallow cumulus convection: an overview

In current GCMs, the spatial and temporal resolution is far from sufficiently resolving convection. Thus, convection and clouds are treated as sub-grid scale processes and are parameterized. Besides the practical needs of parameterizing convection in GCMs, developing and improving simple models of convection has its own merit: it reflects our current understanding of convective dynamics and the way we describe it mathematically.

In this Section, I first introduce the bulk entraining/detraining plume model, which is a very basic and widely-used model in GCMs. Then, using the bulk entraining/detraining plume model as a starting point, I examine the key assumptions, compare this model with some other cloud models, and discuss the entraining mixing process in convection.

1.2.1 Bulk entraining/detraining plume model

Interestingly, the first scientifically influential cloud model (based on the author's best knowledge) is proposed by an oceanographer, Henry Stommel (Stommel 1947). In his vision, a convective cloud resembles a rising plume that continuously entrains environmental air. The Stommel model can be written in the following way (with some other assumptions that will be discussed later):

$$\frac{1}{M}\frac{\partial M}{\partial z} = \varepsilon , \tag{1.1}$$

$$\frac{\partial \phi_c}{\partial z} = -\varepsilon\left(\phi_c - \phi_e\right) + S_c . \tag{1.2}$$

Equation (1.1) is the mass conservation equation, where M is the mass flux of the plume with units of $kg\, m^{-2} s^{-1}$ and ε is the fractional entrainment rate per distance with units of m^{-1}.

Equation (1.2) is the conservation equation for an arbitrary tracer ϕ (for example, total water

content q_t or liquid water potential temperature θ_l). ϕ_c is the cloudy mean value of ϕ, and ϕ_e is the environmental mean value. S_c is the source/sink term of ϕ inside the cloud.

The Stommel model correctly captures the fact that the dilution of a cloud by entraining environmental air is key to determining the destination of the cloud. However, later with more observational data becoming available (e.g. Warner 1955), Warner pointed out that the Stommel model could not predict the correct cloud top height and the cloud liquid water content simultaneously (Warner 1970). This contradiction, which is called the Warner Paradox, may be easily seen in equation (1.1) and (1.2). There is one free parameter ε but two unknown variables M and ϕ_c. It is not guaranteed that one fractional entrainment rate will satisfy two equations at the same time.

One way to resolve the Warner Paradox is including detrainment in the Stommel model. Tank experiments (e.g. Malkus and Scorer 1955) show that in a stratified environment, as a plume rises, a certain amount of the plume's mass is detached from the plume and left behind. In atmospheric convection, besides the environmental stratification, the evaporation cooling of liquid water in the mixture of cloudy and environmental air introduces another source of negative buoyancy and can further enhance the detrainment. With detrainment in consideration, the model can be written as

$$\frac{1}{M}\frac{\partial M}{\partial z} = \varepsilon - d\,, \tag{1.3}$$

$$\frac{\partial \phi_c}{\partial z} = -\varepsilon\left(\phi_c - \phi_e\right) + S_c\,, \tag{1.4}$$

where d is the fractional detrainment rate per distance. We call this bulk entraining/detraining plume model simply as the "bulk plume model" in the rest of the thesis. Including detrainment in the model adds another degree of freedom to the system, so the model can have both the cloud

top and the liquid water profile right simultaneously.

Another way of resolving the Warner Paradox is expanding the bulk plume into a spectrum of plumes to represent an ensemble of clouds (e.g. Arakawa and Schubert 1974). In a spectral plume representation (more discussion in Section 1.2.4), the cloud top is set by a small fraction of high-reaching plumes whose properties can be significantly different from the averaged properties of all plumes.

A basic function of convective parameterization is to provide convective tendency (which is the vertical convergence of convective flux) to GCMs. In bulk plume models, the tracer flux due to convective transport is usually estimated using the mass flux approximation or the so-called "top-hat" approximation (e.g. Ooyama 1971, Betts 1975). The mass flux approximation assumes that the tracer transport is mainly due to the organized cloudy updraft; the contribution from the environmental turbulence and in-cloud turbulence is small. Under this approximation, the convective flux (F_ϕ) of tracer ϕ in the bulk plume model can be written as

$$F_\phi = M\left(\phi_c - \phi_e\right). \tag{1.5}$$

In shallow cumulus convection, the convective flux using the mass flux approximation captures about 60% to 90% of total tracer flux throughout the cloudy layer (Siebesma and Cuijpers 1995). In deep convection, the approximation is less accurate because it neglects the cloudy downdrafts and other processes. Nevertheless, it is also widely used in deep convective parameterizations (e.g. Tiedtke 1989) and some dry boundary layer parameterizations (e.g. Wyngaard and Moeng 1992).

The bulk plume model is successful in modeling shallow cumulus convection to a certain extent. It is not surprising that lots of operational cloud parameterizations are based on this model framework.

1.2.2 Lateral entrainment or cloud top entrainment

There have been recurring debates about the relative importance of two entraining processes: the lateral entrainment and the cloud top entrainment. The lateral entrainment, as in the bulk plume model, states that a cloud entrains environmental air mainly through its lateral boundaries. The cloud top entrainment (Squires 1958) assumes environmental air is entrained into the cloud mostly through mixing at the cloud top. The two mechanisms, which coexisted in the study of convection for a long time, emphasize on different sources of the entrained environmental air and lead to different pictures of how to model clouds.

The cloud top entrainment might be inspired by the observations of the tortuous turbulence structure associated with the cumulus clouds in the real atmosphere. However, the strongest support was from the analysis of Paluch (1979). Paluch (1979) plotted the sampling points of cloudy air on a 2 dimensional diagram with conserved variables as the x and y-axes of the Paluch diagram. The data points lie close to a straight line that connects the environmental sounding from the cloud base to the cloud top. This non-intuitive result at that time was explained by assuming that most cloudy air is the result of the 2-member mixing between the cloud base and the cloud top air. The physical picture was that: as a cloud rises turbulence mixing at the cloud top generates negatively buoyant air, which descends in the form of cloudy downdrafts and later mixes with cloud updrafts. Similar results on the Paluch diagram are found in many other observational data (e.g. Betts 1982, Lamontagne and Telford 1983). The robustness of Paluch analysis makes the cloud top entrainment view appealing (e.g. Squires and Turner 1962, Blyth 1993).

The tide of debate changes to the lateral entrainment view when alternative interpretations are

assigned to the result of the Paluch analysis. Taylor and Bake (1991) argued that due to the strong regulation of the buoyancy sorting (Raymond and Blyth 1986) the cloudy air can only distribute in a very narrow triangle on the Paluch diagram. The sampling points of cloud that lie inside the narrow triangle region resemble a straight line. Some other studies (e.g. Lin and Arakawa 1997, Heus et al. 2008) looked into this problem by direct tracking the trajectories of air moving in and out of cumulus clouds. Their results show little evidence of cloud top entrainment and further confirmed the dominance of lateral entrainment. With these evidences, the controversy of the lateral entrainment versus the cloud top entrainment seems to be finally settled.

1.2.3 Effective entrainment or direct entrainment

In this subsection, we discuss the two different views of defining lateral entrainment: the effective entrainment and direct entrainment.

In the bulk plume model, it is assumed that the entrained air mass has the same properties as the environmental mean and the detrained cloudy air mass has the same properties as the cloudy mean. Under this assumption, only entrainment but not detrainment can modify the cloudy air properties (this point can be easily seen in equation (1.4)). However, in cumulus convection cloudy air is far from homogeneous. Both observations and Large-eddy simulation (LES) results show that from cloud core to cloud edge cloudy air properties follows a systematic trend (e.g. Heus and Jonker 2008, Jonker *et al.* 2008). The cloud core, which is protected from entraining dilution, is moister, more buoyant and rises faster. The air near cloud edge, which suffers from entraining, is drier, less buoyant, and rises more slowly. Further more, environmental air that is adjacent to the cloud edge (, which is also called the "subsiding shell" (Jonker *et al.* 2008)) has

properties significantly different from the environmental mean.

The above results suggest that the entraining-environmental-mean and detraining-cloudy-mean assumptions are not true in real convection. However, from the budget point of view there is an alternative way of interpreting this assumption. The entrainment in equation (1.3) and (1.4) can be interpreted as the definition of the “effective entrainment”, which is the entrainment if we force the entraining-environmental-mean assumption to hold. The same is true for the “effective detrainment”.

Several studies tried to diagnose a "direct entrainment" by measuring the mass crossing the interface of a cloud (Dawe and Austin 2011a, Romps 2010, Yeo and Romps 2012). Different approaches were applied; for example, Romps (2010) measured the in/out flux of a “cloudy active tracer”, while Yeo and Romps (2012) followed and counted the trajectories of Lagrangian particles (they used a similar Lagrangian particle model as the one used in this thesis, see details in section 1.3.3). Their conclusions generally agree that the direct entrainment is significantly larger than the effective entrainment, by about a factor of 2. This discrepancy between the direct entrainment and effective entrainment is caused by the differences of entrained air properties in these two views: the entrained environmental air in the direct entrainment view has the properties that more resemble the cloudy air (Dawe and Austin 2011b). However, the two definitions of entrainment have the same effect in the tracer budget equation (1.3) to (1.4).

A more meaningful question may be what are the pros and cons of the two definitions. In my point of view, while the studies in the direct entrainment view is definitely valued in revealing the detailed processes during entrainment mixing, the effective entrainment is a more robust definition. During mixing processes, the mass exchange between the environment and clouds should not be viewed separately from the associated tracer exchange. Thus, entrainment is not a

well-defined quantity without specifying a tracer (as it is done in the direct entrainment measurement). The direct entrainment may also depend on the model resolution. As the model resolution increases, the transport of eddies that was parameterized as subgrid-scale diffusion now is explicitly resolved, so the air mass moving in and out of the cloud boundaries increases as well as the measured direct entrainment. The effective entrainment is independent to the model resolution.

It is pointed out that the effective entrainment can have different values for different tracers (e.g. Romps 2010). This tracer dependence is due to the different distributions of tracers in air mass. In shallow convection without precipitation, conserved tracers like q_t and θ_l are so well correlated that the effective entrainments for them are almost identical. However, for other tracers, especially the tracers with sources and/or sinks (for example, reactive chemical tracers), their effective entrainment can differ from the effective entrainment of q_t significantly. This tracer dependence cannot be resolved by using the direct entrainment definition. In the direct entrainment view, although the direct entrainment is measured independently with the tracers, the tracer values of entrained air are different and unknown. How to solve the dependence of entrainment on tracers is an open question.

1.2.4 Bulk plume or multiple plumes

The bulk plume models only use one bulk plume to represent the average of clouds; thus inhomogeneities among cloudy updrafts are neglected. A natural way to preserve the inhomogeneities is to use multiple plumes. A typical multiple plume model (or in its continuous form, a spectrum of plumes as in Arakawa and Schubert (1974)) groups clouds or cloudy updrafts with similar properties together into one bin in a spectrum of plumes. Each type of

plume uses the same conservation equations but with a different effective entrainment rate. Mass exchanges between plumes are not considered. Similar to the idea of the multiple plume models, some multiple parcel models (e.g. Emanuel 1991, Neggers *et al.* 2002), which release many parcels and evolve them individually, are developed. Here, we consider them as the same group and simply call them multiple plume models.

A bulk plume model can be viewed loosely as the sum of all the plumes of a multiple plume model (Yanai *et al.* 1973, Arakawa and Schubert 1974). Although studies point out that due to the nonlinear processes, this simple summation may be not mathematically precise (Plant 2010), the error is generally tolerable and many times fortuitously cancels with other errors (Lin and Arakawa 1997).

Whether to use a bulk plume or multiple plumes to represent clouds is the first decision one has to make at the beginning of developing a cloud model. While the choice may depend on the philosophy of model developers, the two schools of models have different features that are attractive in different aspects.

Many current operational convective parameterizations are based on the bulk plume models. One reason may be the consideration of computing power back to the days when the models were developed. However, this is not an issue anymore today. Perhaps the more important reason for its popularity is that the bulk plume model is simple to understand and easy to control. The climatology of GCMs is sensitive to the details of convective parameterizations (e.g. Tiedtke 1989). The bulk plume model allows the modelers to reduce the biases of GCMs' climatology relatively easy by tuning or adding modifications in certain directions. The multiple plume models, due to the complex structures and interactions between different components, usually are more difficult for the modelers to manipulate than the bulk plume models.

Despite the practical considerations for GCMs, the most important advantage of a multiple plume model is that it preserves the inhomogeneities among cloudy updrafts. The preservation of inhomogeneities is important in cloud microphysics that nonlinearly depend on the thermodynamical states of cloudy air. A bulk plume model neglects the nonlinearities and cannot be used with sophisticated microphysics schemes. It is suggested that in the future climate models, eventually clouds will be parameterized in the multiple plume form (Yano *et al.* 2013). The updrafts' inhomogeneities can also be important in convective transportation of chemical tracers (e.g. Lawrence and Rasch 2005) and the associated reactions. Recently, more multiple plume models have been proposed (e.g. Cheinet 2003, Sušelj *et al*. 2012, Sušelj *et al.* 2013); that seems to indicate the shifting trend.

In Chapter 4 of this thesis, I extend the basic concept of entrainment rate in bulk plume models and propose a framework for diagnosing mixing in multiple plume/parcel models.

1.2.5 Homogenous entrainment, inhomogeneous entrainment and stochastic entrainment

The bulk plume model assumes that entrainment is a continuous process in time. It also assumes entrained environmental air mixes with cloudy air homogenously. This is another oversimplified assumption in the bulk plume model.

In cumulus convection, entrainment usually occurs as episodic pulses and in the form of strands or gulps. The observational support of inhomogeneous entrainment can be seen by sampling cloud with aircrafts. The sampling shows large temporal and spatial variations of cloudy air. The segments of cloudy air with homogeneous properties are usually separated by patches of air with properties close to environmental air (e.g. Austin *et al.* 1985). This indicates that entrained blobs

of environment air is not instantaneously mixed with the rest of the cloudy air. It takes a certain amount of time for them to mix with each other, during which period other entrainment events may occur and generate new dry air patches in the cloud. Another piece of indirect but more quantitative evidence of inhomogeneous mixing comes from the calculation of the cloud drop size distribution (e.g. Houze 1993). Because smaller droplets grow faster than larger droplets, under a homogenous entrainment assumption the cloud drop size distribution should become narrower as the sampling height goes up. However, the observed cloud drop size distribution has a relative constant width with height. Using a discontinuous and inhomogeneous entrainment can resolve the contradiction of cloud drop size distribution between the theoretical calculation and observations (e.g. Houze 1993).

Several approaches are proposed to represent the inhomogeneous entrainment in simple models. As a modified version of the bulk plume models, the buoyancy-sorting models partly take the inhomogeneity during entrainment into account (e.g. Raymond and Blyth 1986, Zhao and Austin 2003, Bretherton *et al.* 2004). In these models, when a mixing event occurs, a spectrum of mixtures is generated following a certain probability distribution function (PDF, see some choices of the PDF in Zhao and Austin 2003). Depending on the ratio between environmental air and cloudy air, some of the mixtures are positively buoyant and the others are negatively buoyant. The buoyancy-sorting mechanism assumes that the positively buoyant mixtures are incorporated into the cloud as entrainment and negatively buoyant mixtures are detached from the cloud as detrainment. In other words, instead of prescribing ε and d as some bulk plume models (e.g. Siebesma and Holtslag 1996), a buoyancy-sorting model determines the ε and d interactively with the environment by the buoyancy-sorting mechanism. However, the inhomogeneous mixtures in the buoyancy-sorting models only exist temporarily. The models

assume the in-cloud turbulence is sufficiently strong that it instantaneously homogenizes all cloudy air right after the buoyancy-sorting process. The buoyancy-sorting mechanism is also introduced in the multiple plume framework (Emanuel 1991, Zhao and Austin 2003), which release the above assumption of infinitely strong in-cloud mixing. Krueger *et al.* (1997) suggested that the inhomogeneous entrainment process might be modeled by randomly shuffling cloudy air and at the same time applying some diffusion mixing. This method allows for a in-cloud mixing with finite strength, which is closer to real convection.

Recent studies further suggest that entrainment may be better represented as a stochastic processes. Romps and Kuang (2010) found that the variation of cloudy updrafts cannot be explained by the initial variation among updrafts at cloud base. It is mostly due to the variation introduced during the entrainment events. They suggest that entrainment should be modeled as discrete and episodic events, and the strength of entrainment events should follow certain probability distributions. By using a "purity tracer", they found a probability distribution function that best matches the results of a simple parcel model and LES. This stochastic entrainment is supported by some observational studies (Lu *et al.* 2012) and is applied in some other simple cloud models (e.g. Sušelj *et al.* 2013).

1.3 Models and tools

1.3.1 Cloud resolving models and Large-eddy simulations

The amount and data types from cloud observations are limited, and sometimes the data quality is arguable. As many other fields in the atmospheric sciences, numerical simulations are used as virtual field campaigning. Depending on the scale of convective eddies, Cloud Resolving Models (CRM, usually appropriate for tropical convection studies) and LES (usually appropriate for convective boundary layer and boundary layer cloud studies) have been proven to be very powerful tools.

CRM/LES can provide a set of high temporal and spatial resolution data, which can be used for diagnostic studies, or simple visualizations. The work of Heus *et al*. (2009) is one example showing how one can exploit the LES to inspect convection innovatively. To have the life cycle composites of cumulus clouds, they put the LES simulated cloud in a virtual reality environment and combine both automatic identification and human inspection to select certain types of clouds.

CRM/LES has applications on a wide range of topics. Below I only list some examples of the usage of CRM/LES to highlight its capability. To test the fixed anvil temperature hypothesis, Kuang and Hartmann (2007) ran a series of radiative-convective equilibrium experiments with different sea surface temperature (SST), CO_2 and O_3 concentrations. The results confirm the hypothesis and lend theoretical support to the positive climate feedback of high clouds in climate simulations (e.g. Zelinka *et al.* 2013). As another example, Böing *et al.* (2012) artificially smoothed the properties of boundary layer air to test the effect of cold pool organization on convection. Not limited in meteorology, CRM/LES can help in the parameterization of convective transport of chemical tracers in chemical transport models or GCMs (e.g. Gustafson

et al. 2008), or to clarify persisting confusion in observations of isotopic tracers (Moore *et al.* 2013). As shown in the above examples, CRM/LES allows one to design idealized experiments to isolate a single process that is buried in other complicated processes, to break a chain of feedback loops, to test the limit of current theory, and so on.

Two LES models, the Das Atmospharische Modell (DAM, Chapter 2 and 3) and the System for Atmospheric Modeling (SAM, Chapter 4) model are used in this study.

1.3.2 Linear response functions

One creative way of using CRM/LES is the convective linear response functions (LRFs, Kuang 2010). Let us consider a convective ensemble in an equilibrium or reference state, for example radiative-convective equilibrium. Its responses to an infinitesimal perturbation can be written as the following linearized matrix equation:

$$\frac{dX}{dt} = L_{RF} X \quad . \tag{1.6}$$

In the above equation, X is the state vector that fully describes the convective system. L_{RF} is the linear response function matrix.

At first glance, equation (1.6) seems only a mathematic practice of the perturbation expansion. However, Kuang (2010) found that for the purpose of modeling convectively coupled tropical waves (a) the environmental temperature and moisture can fully describe the system; (b) the linearized equation is accurate enough for sizeable perturbations. Here, a sizeable perturbation means its amplitude is comparable to the typical perturbations of the convectively coupled tropical waves. Point (a) reduces the number of the variables in the state vector X to two, greatly simplifying the system. Point (b) ensures that the LRFs are practically useful. One has to keep in mind that point (a) and (b) are not guaranteed for every dynamical system. Here it means that

although moist convection is a complex system with lots of highly nonlinear processes, the overall responses of a convective ensemble can be relatively linear.

By perturbing the convective system with a sufficiently complete set of perturbations in a CRM and then solving the matrix equation (1.6), Kuang (2010) was able to calculate L_{RF}. He verified that the convectively coupled tropical waves that are modeled using the LRFs generally matched the observations.

With the above argument, the LRFs now have deep meanings and can serve as a powerful tool in the study of convection. The LRFs fully describes the dynamics of the system around the reference state. It can serve as phenomenological but relatively accurate parameterizations. Kuang (2010) suggested using the LRF or the LRF method to (1) understand the physical processes behind the convective responses (as in Nie and Kuang 2012a, b); (2) to guide and improve convective parameterizations (as in Herman and Kuang 2013); and (3) to understand the interaction between tropical large-scale circulation and convection (as in Kuang 2011, 2012).

In the study of this thesis, I explore the dynamics of shallow cumulus convection by examining its responses to large-scale temperature and moisture perturbations using the LES and a stochastic parcel model.

1.3.3 the Lagrangian particle dispersion model

The idea of advecting Lagrangian particles using simulated velocity fields has many applications, such as identifying the source of water vapor (e.g. Stohl and James 2005), studying the long distance transport of chemical pollutants (e.g. Li *et al.* 2002), and so on. In Chapter 4, I use a Lagrangian particle dispersion model (LPDM) to investigate the mixing in shallow cumulus convection. The LPDM is similar to the model in Weil *et al.* (2004) and Heus *et al.*

(2008). Initially, a large number of massless particles are randomly released in each grid box of the CRM/LES that the LPDM is embedded in. The particles are then advected around by the CRM/LES resolved winds. The trajectories of these particles and the thermodynamics and dynamics properties contain the information of cumulus dynamics. As an example, figure 1-1 plots the trajectories of Lagrangian particles in a shallow cumulus convection ensemble during a period of half an hour. In the figure, clouds and updrafts are easily seen as clusters of particles rising from cloud base. Some of the particles detrain at lower heights while others rise to the inversion layer with a large amount of liquid water condensation (indicated by red color). How to extract valuable information from the particles' trajectories is the key question when one is designing the experiments using the LPDM.

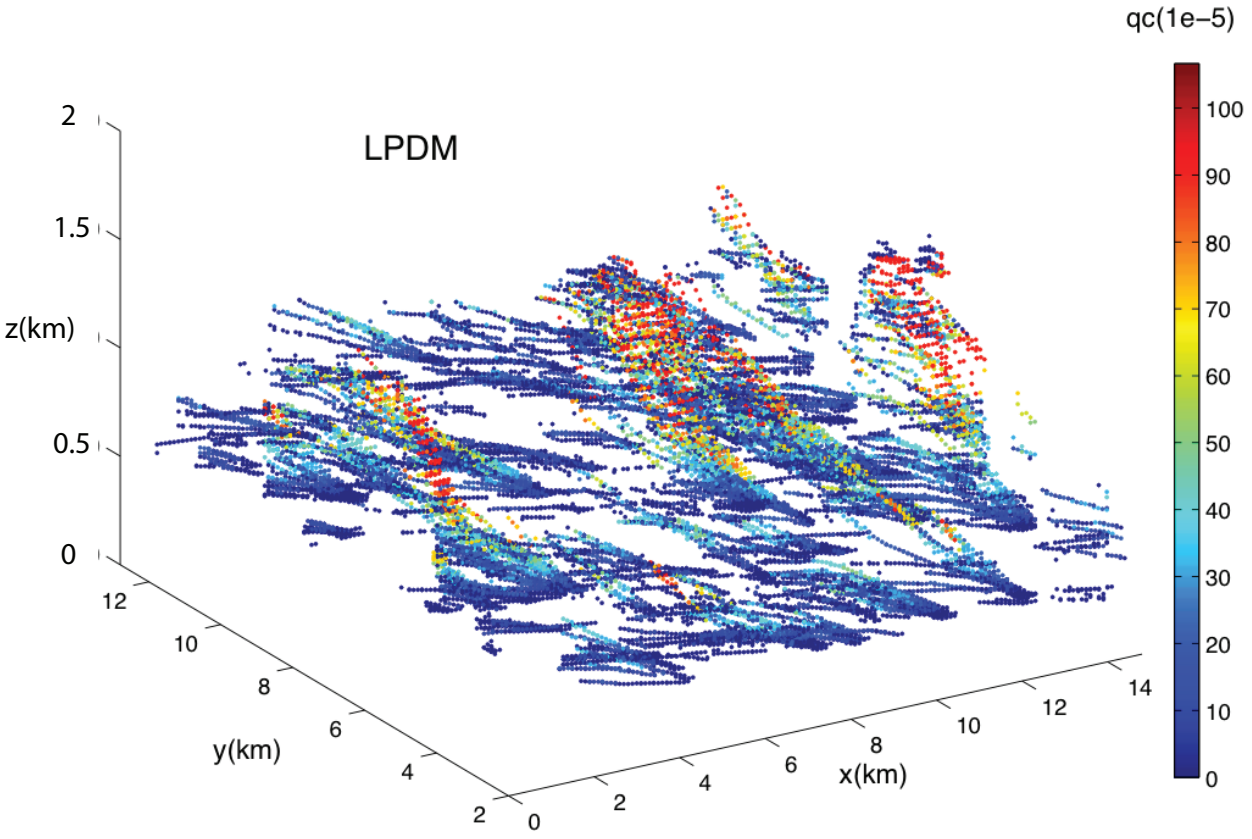

Figure 1-1: The trajectories of Lagrangian particles given by the LPDM for a LES simulation of shallow cumulus convection. The trajectories are shown when the particles are in cloudy grids. The color shows the liquid water content of the particles with a unit of $kg\ kg^{-1}$.

1.4 Outline of this thesis

In Chapter 2, we study the responses of shallow cumulus convection to large-scale temperature and moisture perturbations. We examine the updrafts' properties with and without the perturbation and match the results between LES and a simple parcel model. Analyzing the evolution of parcels in the simple parcel model reveals the underlying processes during the responses. This work has been published in Nie and Kuang (2012a). In Chapter 3, we further develop the stochastic entraining parcel model into a convective parameterization. This is done by extending the releasing level of the parcels from the cloud base down to the surface. This work has been published in Nie and Kuang (2012a). In Chapter 4, we propose a new mapping framework for diagnosing mixing in cumulus convection. The mapping matrices, which are constructed using the Lagrangian particle dispersion model, describe the mixing characteristics and provide a reference against which multiple-parcel models can be compared with. This work has been published in Nie and Kuang (2012b). Finally, in Chapter 5, we close with conclusions and future prospects.

CHAPTER 2

RESPONSES OF SHALLOW CUMULUS CONVECTION TO LARGE-SCALE TEMPERATURE AND MOISTURE PERTURBATIONS

Responses of shallow cumuli to large-scale temperature/moisture perturbations are examined through diagnostics of Large-eddy-simulations of the undisturbed Barbados Oceanographic and Meteorological Experiment (BOMEX) case and a stochastic parcel model. The perturbations are added instantaneously and allowed to evolve freely afterwards. The parcel model reproduces most of the changes in the LES-simulated cloudy updraft statistics in response to the perturbations. Analyses of parcel histories show that a positive temperature perturbation forms a buoyancy barrier, which preferentially eliminates parcels that start with lower equivalent potential temperature or have experienced heavy entrainment. Besides the amount of entrainment, the height at which parcels entrain is also important in determining their fate. Parcels entraining at higher altitudes are more likely to overcome the buoyancy barrier than those entraining at lower altitudes. Stochastic entrainment is key for the parcel model to reproduce the LES results. Responses to environmental moisture perturbations are quite small compared to those to temperature perturbations, because changing environmental moisture is ineffective in modifying buoyancy in the BOMEX shallow cumulus case.

2.1 Introduction

As motivated in Chapter 1, it is important to understand the dynamics of shallow cumulus convection and to better parameterize it in GCMs. Our strategy to better understand shallow cumuli is to look at how they respond to small perturbations to their large-scale environment. This approach has been applied previously to deep convection (Mapes 2004, Kuang 2010, Tulich and Mapes 2010, Raymond and Herman 2011). Kuang (2010) was able to determine the responses of convection (using a CRM) to a sufficiently complete set of perturbations in their large-scale environment, and use these responses to approximate the behavior of convection near a reference state. A range of interesting behaviors was found, such as stronger sensitivity of convection to temperature perturbations in the lower troposphere than those in the upper troposphere (Kuang 2010, Tulich and Mapes 2010, Raymond and Herman 2011). The physical processes behind the responses however are not yet fully understood (Kuang 2010, Tulich and Mapes 2010). In this study, we shall use shallow non-precipitating convection, the dynamics of which are simpler without the many complicating processes associated with precipitation, as a starting point to understand and model the physical processes behind the responses of cumulus convection to large-scale temperature and moisture perturbations.

Despite its relative simplicity, shallow cumulus convection involves interactions among a number of subcomponents, such as the subcloud layer, whose thermodynamic properties and turbulence statistics, together with the strength of convective inhibition, set the properties and the amount of cloudy updrafts at the cloud base; the interactions between clouds and their environment and within the clouds themselves, which determine the evolution of cloudy updrafts as they rise from the cloud base; and the fate of these cloudy updrafts as they penetrate into the inversion layer. These interactions are reflected in the construct of many contemporary

parameterizations (e.g. Bretherton *et al.* 2004, Neggers and Siebesma 2002). In this chapte, we will focus on perturbations in the cloud layer (above the cloud base but below the inversion), thus emphasizing the evolution of cloudy updrafts as they rise from the cloud base. Being able to better study individual processes in isolation is an advantage of looking at responses to small perturbations, as the other subcomponents can be regarded as mostly unchanged.

In addition to how heating and moistening rates averaged over the whole cumulus ensemble change in response to temperature and moisture perturbations, we place special emphases on changes in the statistical distributions of cloudy updrafts. While many of the current shallow schemes are bulk schemes (e.g. Kain and Fritsch 1990, Bretherton *et al.* 2004), it is important to capture the statistical distribution of the cloudy updrafts in order to better simulate microphysics and chemistry beyond the goal of simulating heating and moistening tendencies. This is similar to efforts of probability distribution function (PDF) based parameterizations (e.g. Lappen and Randall 2001, Larson *et al.* 2002, Golaz *et al.* 2002).

We aim to understand changes in the statistical distributions of cloudy updrafts in response to the temperature/moisture perturbations. We will use extensive diagnostics of Large-eddy-simulations with the aid of a tracer-encoding technique. We will then use a stochastic parcel model (SPM) to help interpret the results of the LES. Section 2.2 provides brief introductions to the models and the tracer-encoding technique, as well as a description of the experiments. As we will show in Section 2.3, the SPM reproduces many of the features of the LES-simulated shallow convection and its responses to temperature and moisture perturbations. We then investigate the evolution history of the parcels in the SPM to identify the physical processes behind the responses (Section 2.3). In Section 2.4, we summarize the results of this chapter.

2.2 Models and Experimental Design

2.2.1 The tracer encoding technique

The LES model used here is Das Atmospharische Modell (DAM, Romps 2008). It is a three-dimensional, finite-volume, fully compressible, nonhydrostatic, cloud-resolving model. We use a tracer encoding technique to infer the history of cloudy updrafts (Romps and Kuang 2010 a,b). Two artificial tracers, called purity and the equivalent potential temperature tracer ($\theta_{e,tracer}$), are released at a specified height (tracer release height, $Z_{release}$). At and below $Z_{release}$, the purity tracer is always set to 1 and $\theta_{e,tracer}$ of a grid point is always set to its equivalent potential temperature θ_e. The two tracers are advected in the same way by the model velocity field, and at every time step, both tracers are set to zero for grid points not in the vicinity of cloudy updrafts (cloudy updrafts are defined here as grid points with liquid water content q_l greater than $0.01\ g\ kg^{-1}$ and vertical velocity w greater than 0.5 $m\ s^{-1}$). A grid point is considered to be in the vicinity of cloudy updrafts if it is within a 3 grid point distance from any cloudy updrafts. By reading the value of these tracers at some level above $Z_{release}$, one can infer some aspects of the updraft's history: the purity tracer estimates the total amount of environmental air entrained, while the ratio of $\theta_{e,tracer}$ and purity gives the updraft's equivalent potential temperature θ_e value at $Z_{release}$. We shall refer to this ratio as "$\theta_{e,ed}$", which stands for encoded equivalent potential temperature. The readers are referred to the above references for some examples of the usages of the tracer encoding technique (e.g. section 2 of Romps and Kuang (2010b)).

2.2.2 The stochastic parcel model

We shall also use the stochastic parcel model developed in Romps and Kuang (2010a,b) to help understand the results from the LES. This model integrates, forward in time (τ), the prognostic equations of parcel properties (height $z(\tau)$, volume $V(\tau)$, temperature $T(\tau)$, water vapor content $q_v(\tau)$, liquid-water content $q_l(\tau)$, and vertical velocity $w(\tau)$), given the environmental soundings (temperature $T_{en}(z)$ and moisture $q_{v,en}(z)$, where the subscript $_{en}$ denotes an environmental variable), and the initial conditions of the parcels. In this chapter, we set the drag coefficient to zero so that updraft velocity is affected only by buoyancy and entrainment. This is done here solely for simplicity, although there have been arguments made for clouds being slippery thermals that experience little drag Sherwood *et al.* 2010). The parcel model uses a stochastic entrainment scheme. More specifically, the probability that a moving parcel entrains after a time step $\Delta\tau$ is

$$P = \Delta\tau |w| / \lambda, \tag{2.1}$$

where λ is the e-folding entrainment distance. When entrainment occurs, the ratio of the entrained environmental air mass to the parcel's mass (f) has the following probability distribution:

$$\frac{1}{\sigma} e^{-f/\sigma}, \tag{2.2}$$

where σ is the mean ratio of the entrained mass. Because entrainment is stochastic, a large number of parcels are required to cover the full range of entrainment scenarios in order to obtain statistically significant results.

2.2.3 Experimental design

The shallow cumulus system that we study here is a well-studied oceanic trade cumulus case from the Barbados Oceanographic and Meteorological Experiment (BOMEX). The LES runs have a horizontal and vertical resolution of 25m, with a horizontal domain size of 12.8km × 12.8km and a vertical extent of 3km. It is initialized using the initial profiles of temperature, water vapor and horizontal velocities described in Siebesma and Cuijpers (1995), with some small random noises. The radiative cooling and other large-scale forcing are also prescribed as in Siebesma and Cuijpers (1995). A bulk parameterization with a drag coefficient of 1.4×10^{-3} is used to calculate the surface fluxes off the $300.4\ K$ ocean surface. Precipitation processes are turned off. The first 3 hours of the model run are discarded as spin-up. Over the following 2 hours, snapshots are saved every 10 minutes. We then add a temperature or moisture perturbation to each of these snapshots and use them as initial conditions for the perturbed runs. In this way, we produce an ensemble of control and perturbed runs with different initial conditions.

We then diagnose the differences between the ensemble averages of the control runs and the perturbed runs.

Three representative perturbations are studied: a $0.25\ K$ temperature anomaly centered at 987.5m (the T987 case); a $0.5\ K$ temperature anomaly centered at 1262.5m (the T1262 case); and a $0.2\ g\ kg^{-1}$ moisture anomaly centered at 987.5m (the Q987 case). The perturbations added are horizontally uniform and Gaussian-shaped in height with a half width of 75m. The tails of the Gaussian-shaped anomaly are truncated at levels more than 200m away from the center. The perturbations are added instantaneously and allowed to evolve freely afterwards. Our choice of the size of the perturbations was constrained by the desire to obtain statistically robust results (given the computational constraints) and to limit the extent of nonlinearity. For each case, we have done both runs with positive perturbations and runs with negative perturbations, and the

extent of nonlinearity is found to be small. For the T987 case, we have also done runs with a $0.5\,K$ temperature perturbation, which give very similar results to those with a $0.25\,K$ perturbation (times a factor of 2). The only difference is that a peak amplitude of $0.5\,K$ perturbation over 75m represent a change in stratification that is sufficiently strong to be comparable to the background stratification at this height.

This weakens the vertical stratification substantially over the upper half of the perturbation, leading to a local overturning circulation that gives rise to a weak dipole response around 1100m in the moisture field over the first half hour. To avoid this nonlinearity and for ease of comparison with other cases, we present the results with the $0.25\,K$ perturbation but multiply them by a factor of 2 (figure 2-1). As an example, figure 2-1a also shows the positive temperature anomaly for the T987 case. The results shown in next section are the averages of 9 members with positive and negative perturbations.

There is one complication with calculating convective responses to perturbations in DAM: as the temperature and moisture perturbations disrupt this balance, the model adjusts to regain hydrostatic balance. The main effect of this adjustment is an instantaneous adiabatic cooling of the layer after the positive temperature and moisture anomalies are added. For temperature perturbations, this cooling is negligible. However, as we will show in Section 2.3.4, convective heating responses to moisture perturbations are remarkably small and the temperature change associated with the hydrostatic adjustment becomes noticeable. We ran DAM in a single column setting to calculate the cooling from this hydrostatic adjustment and corrected for this effect in the results that we present.

We bin the cloudy updrafts based on their purity and $\theta_{e,ed}$ to produce two-dimensional distributions of their properties as functions of those two variables. Taking the T987 case for

example, in the LES, the purity and θ_e tracers are released at $Z_{release} = 762.5\,m$ (For the T1262 case, $Z_{release} = 1037.5\,m$, and for the Q987 case, $Z_{release} = 762.5\,m$). We then sample cloudy updrafts at $Z_{sample} = 1212.5\,m$ (For the T1262 case, $Z_{sample} = 1487.5\,m$, and for the Q987 case, $Z_{sample} = 1212.5\,m$) for the 1 hour period following the introduction of the anomaly. We then calculate the total mass flux, the mean w and θ_e of all cloudy updrafts inside each bin defined by the purity and $\theta_{e,ed}$ values. These distributions (figure 2-2a to c) provide information on the history of the updrafts traveling through the layer between $Z_{release}$ and Z_{sample}. The sampling period of the first hour is long enough to give statistically significant results but not too long for the added anomaly to have evolved heavily through convective adjustment. During this period, the properties of the cloudy updrafts at $Z_{release}$ are roughly the same for the control runs and the perturbed runs. Therefore, differences in the distributions at Z_{sample} (figure 2-3a to c) give responses of cloudy updrafts to the introduced temperature anomaly.

We compute the same diagnostics for the SPM. The parcels in the SPM are viewed as analogs of the cloudy updraft grid points in the LES. Millions (1 millions in this study) of parcels are released at $Z_{release}$ in the SPM. Two conditions need to be specified for the SPM: the initial conditions at $Z_{release}$ and environmental profiles between $Z_{release}$ and Z_{sample}. To assign them appropriate initial conditions, we sample 100 LES snapshots to get a 3-demensional (3D) PDF of the cloudy updrafts at $Z_{release}$ as functions of w, T, and q_t. The PDFs at $Z_{release}$ from the LES are found to be similar between the control and the perturbed runs. In the SPM, we shall use the PDFs from the LES control runs for both the control and the perturbation runs. The initial conditions of the parcels are drawn randomly from this 3D PDF. This procedure ensures that the parcels in the SPM have the same statistical properties as updrafts in the LES at $Z_{release}$. For the

control run of the SPM, the environmental sounding is the ensemble mean sounding of the LES control runs.

For the perturbed runs of the SPM, we add the same perturbations as in the LES perturbation runs. We also follow the same sampling processes at Z_{sample}. In the SPM, the purity of a parcel is the ratio of its mass at $Z_{release}$ to its mass at Z_{sample}, and parcels' initial θ_e at $Z_{release}$ takes the place of $\theta_{e,ed}$ in the LES. In the figure axes, we call it "initial θ_e" to remind readers that it is SPM-generated results.

Because the pair of parameters (λ, σ) mainly controls the entrainment process, we briefly discuss how they are chosen. Romps and Kuang (2010b) surveyed a large range of combinations of λ and σ. They defined an objective function based on mass flux agreement between the LES and the SPM and searched the best fitting λ and σ, which are $\lambda = 226\,m$ and $\sigma = 0.91$, that minimizes the objective function. They also note that there is a valley in the (λ, σ) space, where pairs of (λ, σ) give very similar values of the objective function. For pairs of parameters that are along this valley, although the total amount of mass flux is similar, the distribution of mass flux in terms of purity is quite different. For example, the parameters used in Romps and Kuang (2010b) allow too many undiluted updrafts compared to the distributions from our current 25 meter resolution run (figure 2-2a), even though their parameters are consistent with the total amount of mass flux and purity. We have chosen $\lambda = 125\,m$ and $\sigma = 0.32$ to give a mass flux distribution as a function of purity (figure 2-2d) that matches the distribution from the current LES simulations (figure 2-2a).

2.3 Response to Temperature and Moisture Perturbations

2.3.1 Responses in the T987 case

For a temperature perturbation centered at 987.5 meters, the amplitude of the initially added temperature anomaly decreases by a factor of 2 in about 30 minutes (figure 2-1b), an example of the convective adjustment process. In addition, there is slight warming in the trade inversion around 1600m. Moisture responses (figure 2-1c) show that layers below 987.5m experience moistening and layers above experience drying. The moistening propagates downward towards the surface with time. The basic features of the responses can be understood in terms of inhibition of cloudy updrafts by the added temperature anomaly, which cools this region and reduces the initial temperature perturbation. The reduced penetrative entrainment in the inversion layer also leads to the warming near 1600m. Furthermore, the enhanced detrainment in and below the region of the temperature perturbation leads to the moistening, while the reduced detrainment above leads to the drying.

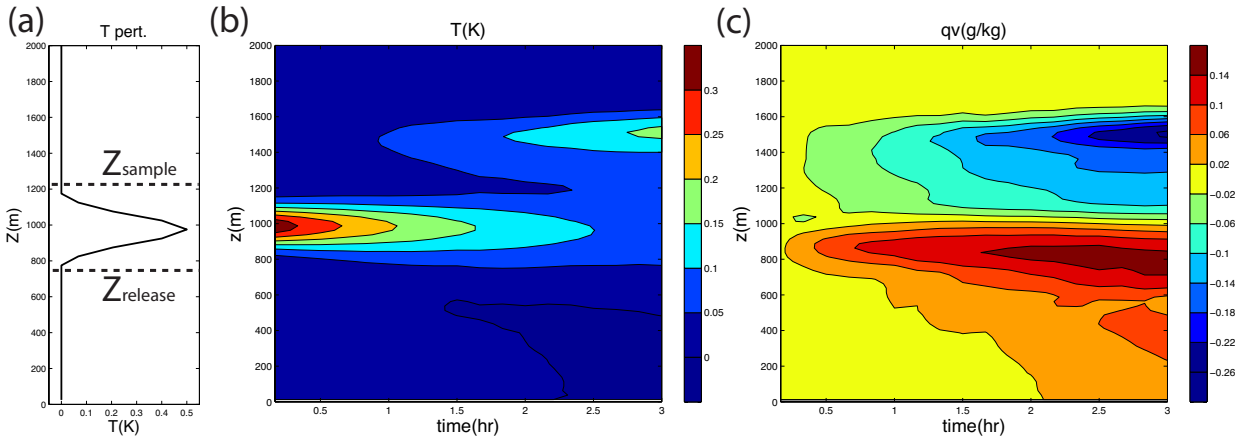

Figure 2-1: (a): The initial temperature anomaly of the T987 case. The heights of $Z_{release}$ and Z_{sample} are also marked. Evolutions of (b) temperature and (c) moisture anomalies after the initial temperature perturbation is introduced. The results are for 0.25K temperature anomalies and are multiplied by 2 for the plotting.

We now investigate changes in the statistics of cloudy updrafts. The mass flux distribution of the LES control run (figure 2-2a) is mostly located between 347.5K and 349.5K on the $\theta_{e,ed}$ axis, reflecting variations of updrafts' properties at $Z_{release}$. The mass flux is mostly located between 0.2 and 1.0 on the purity axis, while the maximum lies around 0.45. This indicates that most updrafts mix with environmental air when they go across the layer between $Z_{release}$ and Z_{sample}. However, there are some undiluted updrafts with purity close to 1 (Here "undiluted" is relative to $Z_{release}$ not to the cloud base). The SPM-generated mass flux distributions (figure 2-2d) show general similarities. We find that the LES mass flux distribution has a narrower range in $\theta_{e,ed}$ than that of the SPM. The narrowing is due to in-cloud mixing in the LES, which homogenizes the initial identities of the air that makes up the updrafts. In our SPM, in-cloud mixing is not included at the moment for simplicity. In-cloud mixing is a process that we would like to add into the SPM in the future, perhaps following the approach Krueger *et al.* (1997).

The distributions of the LES simulated w and θ_e are plotted in figure 2-2b,c. Both θ_e and w show a tilted structure with their values increasing from the bottom-left to the upper-right of the figures. This is simply because parcels that initially have higher $\theta_{e,ed}$ or entrain less environmental air (thus have higher purity) will end up with higher θ_e and also achieve higher w values due to stronger buoyancy acceleration and less slowdown by entrainment. We have also plotted the same distributions for total water content q_t and buoyancy b. They show similar tilted patterns as θ_e (figures are not shown).

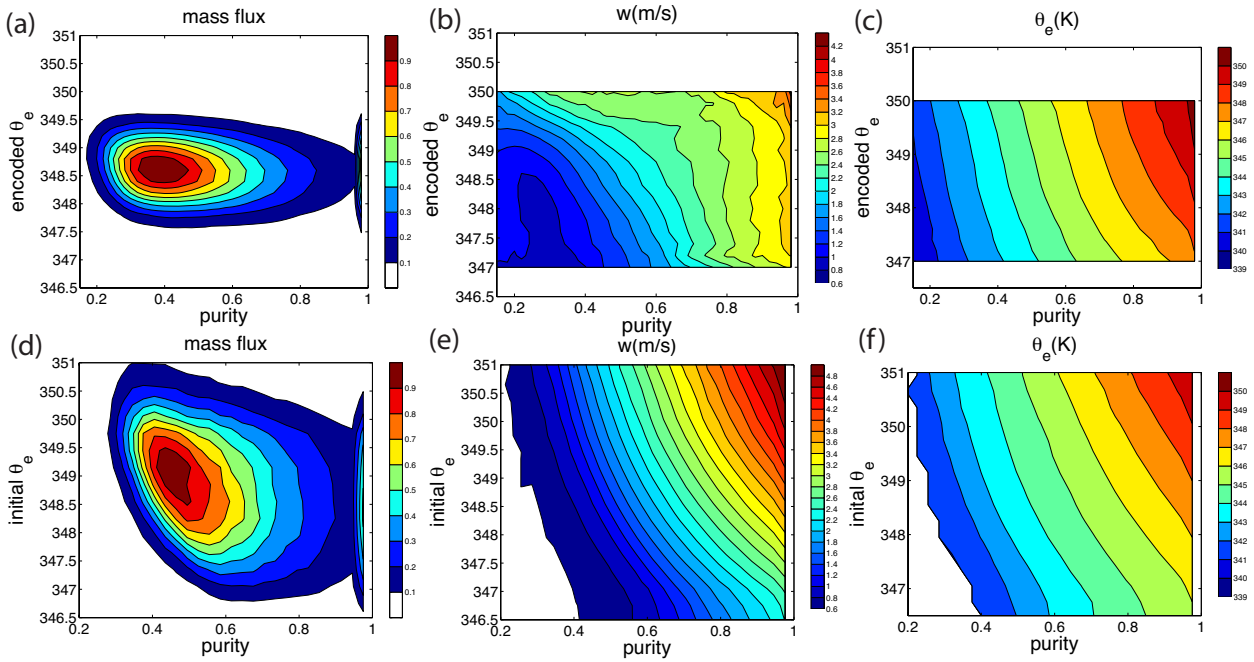

Figure 2-2: (a) - (c): Cloudy updraft statistics of the LES control run: (a) mass flux, (b) w and (c) θ_e shown as functions of purity and $\theta_{e,ed}$. The mass flux distributions are normalized to range from 0 to 1. (d) - (f) are same as (a) - (c) but for results from the SPM control run.

The SPM-generated w and θ_e distributions (figure 2-2e to f) show a similar gradient. Closer inspection shows that the agreement in w is not as good as that in θ_e. More specifically, the constant w contours of the LES distribution are almost vertical in regions of high purity (figure 2-2b), indicating little dependence of w on the encoded θ_e. For high encoded-θ_e values, the dependence of w on purity is also somewhat weakened (constant w contours being more horizontal).

We speculate that the discrepancy between the LES and the SPM (figure 2-2b and 2-2e) is because of the intra-cloud interaction between cloudy updrafts. In our LES simulations, the resolution is relatively high and clouds are well resolved. The cloudy parcels can exchange momentum through pressure gradient force in addition to actual mixing of fluids. This could cause momentum exchange between the most active cloud cores (which tend to be binned into the upper-right corner in figure 2-2b) and the cloudy parcels surrounding them (which tend to be binned into the upper-left and lower-right parts in figure 2-2b), while keeping their thermodynamic properties such as θ_e unchanged.

Several additional LES runs are designed to test our hypothesis (Appendix A). We have tried coarsening the 3D outputs to a lower resolution before generating the statistics shown in figure 2-2a-c (the R25-b runs listed in Table A1). We have also made runs with the same settings as the control but at lower resolutions (the R100 runs listed in Table A1). In both cases (the first and fourth rows in figure A1), the w distribution is more similar to the SPM results and to that of θ_e. On the other hand, runs with higher resolutions (also described in the appendix A, and shown in the third row in figure A1) give results similar to our control. We speculate that in the lower resolution runs, clouds are less well resolved so that the disparity in the intra-cloud homogenization of momentum and thermodynamic properties is reduced.

To test this idea, we calculate the correlation between w and θ_e for the cloudy updrafts. Using 60 snapshots from the control runs and also 60 snapshots from the low resolution runs (R100 runs as in Table A1), we found that the overall correlation between w and θ_e of the cloudy updrafts is 0.57 for the control runs, while for the low resolution runs, it is 0.75. This is inline with the results that w and θ_e have more similar patterns in the low resolution runs than in the high resolution runs. We have further separated w and θ_e variations into intra-cloud and inter-cloud components. The correlation for inter-cloud variations of w and θ_e are 0.62 for both the control and the low resolution runs, while the correlation for intra-cloud variations is 0.54 for the control runs, significantly smaller than that of the low resolution runs (0.78). While these results are inline with our argument, more detailed studies are clearly needed to fully understand the differences seen between the high and low resolution runs. Note also that in the low-resolution runs, the peak mass flux has a higher purity than that of the control runs (0.6 versus 0.45), indicating reduced entrainment because of the lower resolution.

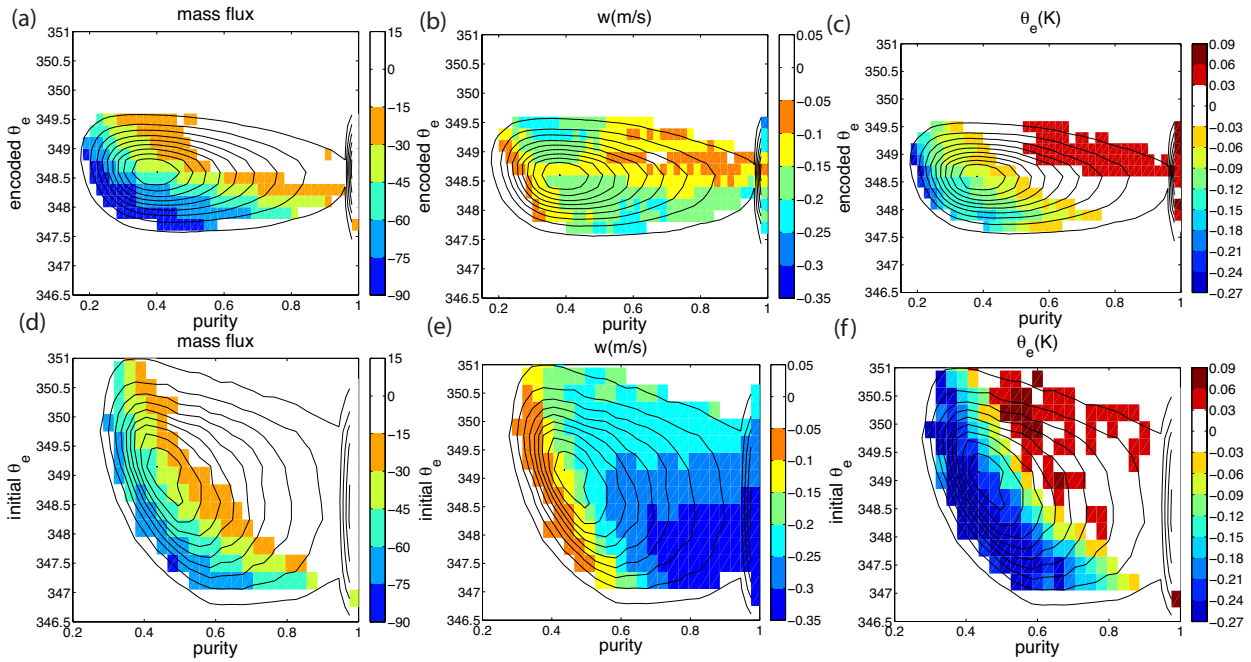

Figure 2-3: (a)-(c): Color indicates LES-simulated fractional changes in mass flux in percent (a), and changes in w (b) and θ_e (c) in the T987 case as functions of purity and $\theta_{e,ed}$. The background black contours are the LES control run mass flux plotted in figure 2-2a. (d) - (f) same as (a) - (c) but for the SPM. The background black contours are the SPM control run mass flux plotted in figure 2-2d. Color values outside the lowest black contour are zeroed out.

Changes in the above statistics in the perturbed runs as compared to the control run are plotted in figure 2-3. Figure 2-3a shows the fractional change in cloudy updraft mass flux in response to the perturbation. It is clear that updrafts with low initial θ_e and those that entrain heavily (thus have low purity) are preferentially removed by the temperature perturbation. The mass flux of updrafts with high initial θ_e and those less diluted by entrainment are less affected. The contours of constant fractional change in mass flux are almost along the contours of θ_e (figure 2-2c), indicating the controlling influence of buoyancy (for saturated air, θ_e is a good proxy for buoyancy): the temperature anomaly forms a buoyancy barrier that preferentially inhibits updrafts with low buoyancy.

Responses in w (figure 2-3b) are negative over most regions, mainly because the temperature perturbation decreases the height-integrated buoyancy (or potential energy) available to the updrafts. The SPM-generated w responses are also all negative. The smaller decrease in w for updrafts with lower purity is because parcels that entrain heavily gain additional buoyancy from the environmental temperature anomaly. The reference state w shown in figure 2-2b,e also affects the w responses. As changes in the height-integrated buoyancy or potential energy available to the updrafts are linearly related to changes in w^2, a higher reference state w implies a smaller change in w for the same change in the height-integrated buoyancy. In regions with strong fractional decrease in mass flux (i.e. the lower-left corner), changes in the height of entrainment events also contribute to the smaller w decrease, as will be discussed in Section 2.3.2.

The less negative patch in the upper-right part of the LES-simulated w responses is not captured by the SPM and is not understood. We speculate that the buoyancy barrier associated with the positive temperature perturbation may inhibit intra-cloud momentum transport and lead to this

less negative patch. More studies into this behavior are clearly needed. Intriguingly, this less negative patch is not seen in the lower resolution LES simulations (not shown).

Cloudy updrafts with high $\theta_{e,ed}$ or high purity (the upper-right part of the PDF), in which there is little mass flux change, show a slight increase in their θ_e due to entrainment of warmer environmental air (figure 2-3c). On the other hand, updrafts with lower $\theta_{e,ed}$ and lower purity (the lower-left part of the PDF), in which there is a significant fractional decrease in mass flux, show a decrease in their θ_e (figure 2-3c,f). The reason for this will be discussed in Section 2.3.2.

The responses of SPM-generated statistics (figure 2-3d-f) are generally similar to those of the LES. Given the simplicity of the SPM and the complexity of the cloud field, we do not expect the SPM to reproduce every feature of the LES statistics (the tracer-encoding technique also has its own deficiencies.) However, the SPM does capture the main responses of statistics, such as the decreases of mass flux in the lower-left region, the general decreases of w, the decreases of θ_e in the lower-left, and the increases of θ_e in the upper-right region.

For a fair comparison with the LES, the evolving soundings during the first hour of the LES perturbation runs were used in the SPM for the results shown in figure 2-3d to f. We have also performed SPM experiments where the environmental soundings are kept constant in time (LES control sounding plus the initial perturbation). The results are very similar to those shown in figure 2-3d to f, except with larger amplitudes (not shown). This is simply because the temperature anomaly in the LES decays significantly over the 1-hour sampling period, instead of maintaining its initial amplitude (figure 2-1b).

The stochasticity of the entrainment process is key for the SPM to match the LES results. To highlight this point, we designed another experiment where we run the SPM with constant entrainment of $\varepsilon = 1.8 \times 10^{-3}\ m^{-1}$ instead of the stochastic entrainment. We choose this constant

entrainment rate to give a similar amount of overall entrainment as in the stochastic entrainment case. For ease of interpretation, in this pair of experiments, we fix the environment sounding to be the initial perturbed sounding to eliminate effects from changes in the environmental sounding. Other settings, such as initial conditions of the parcels are unchanged. Because for the constant entrainment case, the purity of parcels sampled at Z_{sample} is the same, we only plot mass flux distribution as a function of $\theta_{e,ed}$. The PDFs of the SPM with constant entrainment, the SPM with stochastic entrainment, and the LES are shown in figure 2-4 (summing figure 2-2a/d along the purity axis gives the black line in figure 2-4c/b.). With the constant entrainment, the fate of a parcel is determined by its initial conditions. With the temperature perturbation, there is a threshold of around 348.5K in terms of the initial θ_e. Mass fluxes of updrafts with initial θ_e below the threshold are totally cut off, while mass fluxes with initial θ_e above the threshold are not affected at all. The threshold has a finite width because the initial conditions of the updrafts have variations in w, which are not reflected on the initial θ_e axis. On the other hand, the decrease of LES mass flux is over almost all ranges of $\theta_{e,ed}$, although the mass flux with lower $\theta_{e,ed}$ decreases more. The LES results are much more similar to the SPM results with stochastic entrainment (figure 2-4b). This analysis indicates that stochastic entrainment is essential in the parcel model and more realistic than constant entrainment.

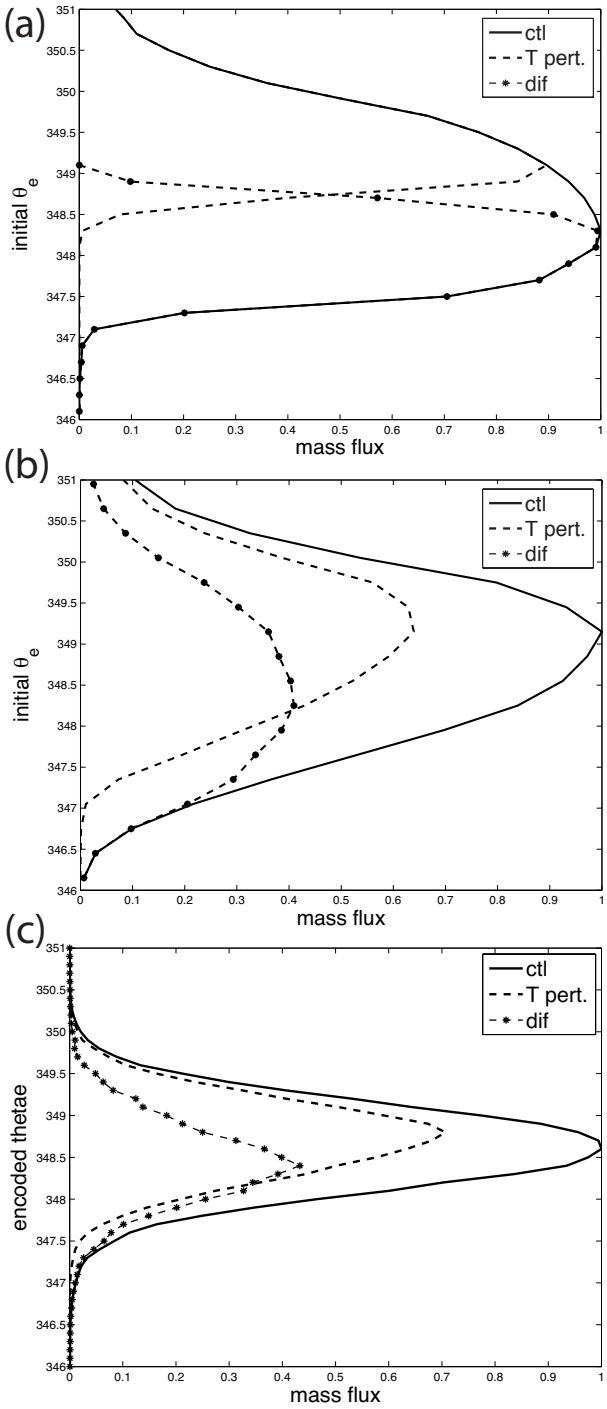

Figure 2-4: The SPM-generated distribution of mass flux as a function of $\theta_{e,ed}$ with (a) constant entrainment and (b) stochastic entrainment. (c) is the LES-generated distributions. The solid and dashed lines represent the control and the perturbed runs, respectively, and the differences are shown in the lines with asterisks.

2.3.2 The height of entrainment

We now analyze the parcels' evolution history in the SPM to understand the decreases of θ_e and their collocation with decreases of mass flux in the lower-left half of figure 2-3c,f. It turns out that decreases of mass flux and composite θ_e are due to one single mechanism.

We plot the trajectories of randomly selected parcels reaching Z_{sample} with a purity of 0.6 in the phase space of Z and purity (figure 2-5). In other words, we are looking at one thin band of the distribution around a purity of 0.6 in figure 2-3d. The purities of parcels at $Z_{release} = 762.5\,m$ are 1 by design. A sudden decline of purity indicates an entrainment event. In the control runs, entrainment events are roughly uniformly distributed in height. However, in the perturbed runs, most parcels reaching Z_{sample} experience entrainment at relatively high altitudes. Since the entrainment probability functions are the same in the control and perturbed runs, we infer that in the perturbed case, the parcels that entrain heavily at lower heights cannot penetrate the perturbation layer to be sampled.

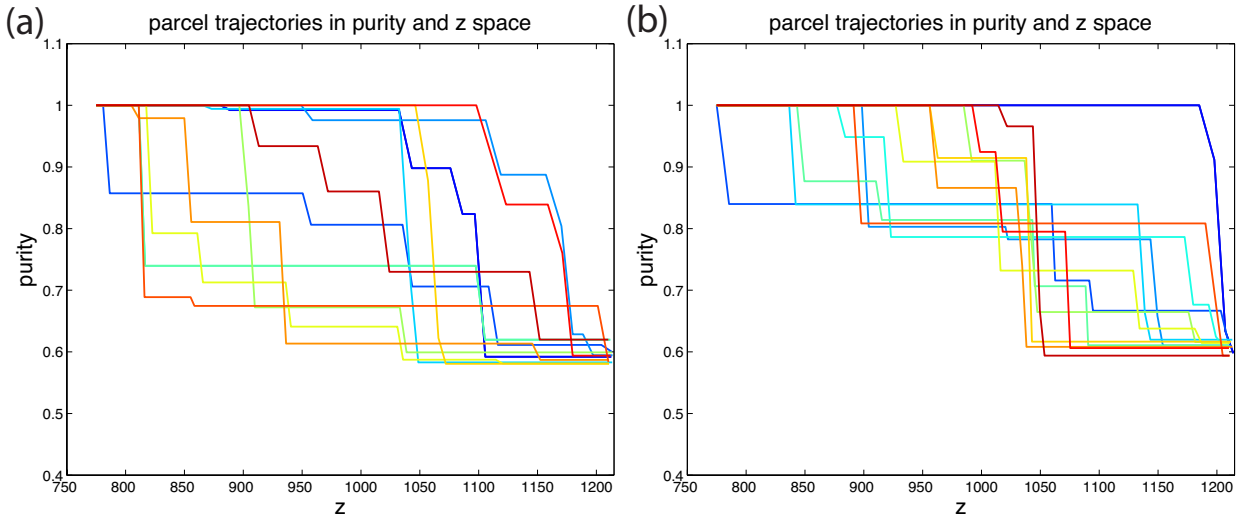

Figure 2-5: The trajectories of parcels with purity between 0.58 and 0.62 at Z_{sample}. Each line represents one trajectory. (a) is for the control run and (b) is for the perturbed run. For each run, only 12 trajectories, which are randomly chosen, are plotted for readability.

The above analysis indicates that the height at which an air parcel entrains is important in determining its fate. To further illustrate this point, we perform the following experiment. We release a parcel at $Z_{release} = 762.5\ m$ with initial conditions of $T = 293.67\ K$, $q_t = 16.82\ g\ kg^{-1}$ and $w = 1.32\ m\ s^{-1}$, which are the mean properties of the cloudy updrafts at $Z_{release}$ in the LES. While traveling toward Z_{sample}, this parcel entrains only once. The single entraining event will dilute the parcel to a purity of 0.6. We release the same parcel a number of times and each time have the parcel entrain at a different height between $Z_{release}$ and Z_{sample}, separated by an interval of 30m. This experiment eliminates variations in the initial conditions. It also simplifies the stochastic entrainment treatment by emphasizing only one aspect: for a parcel that entrains the same amount of environmental air, it may entrain at different heights. In the perturbed run, we again set the environment sounding to be the initial perturbed sounding and keep it constant in time.

We plot the trajectories of these parcels in the phase space of Z and w (figure 2-6). The uppermost line is the trajectory of an undiluted parcel. A sudden decline in w indicates an entrainment event because the parcel entrains environmental air with zero w. For the control run, if the parcel entrains below about 850m, it becomes negatively buoyant and also descends. If it entrains above 850m, it is temporarily negatively buoyant after entrainment. However, after continued ascent by inertia for a certain distance, it becomes positively buoyant and accelerates upward.

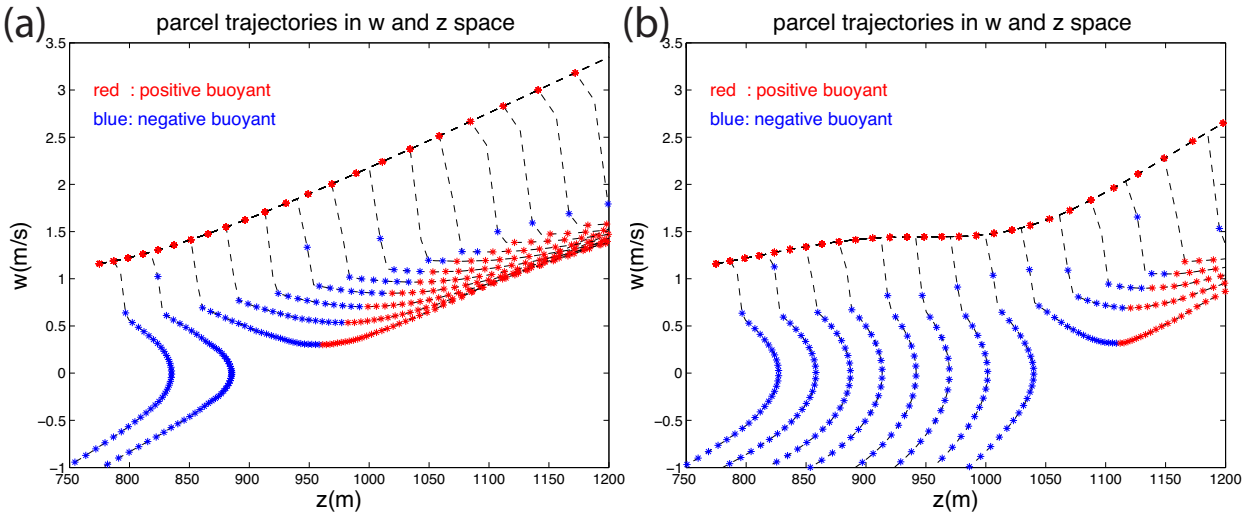

Figure 2-6: The trajectories of parcels that entrain the same amount of environmental air but at different heights. The blue dots indicate negative buoyancy while red dots indicate positive buoyancy. (a) is the control run and (b) is the perturbed run.

With the temperature perturbation, the critical height that separates rising and descending trajectories is higher than that of the control run, reaching about 1035m (figure 2-6b). Thus, in the perturbed run, parcels that entrain at lower altitudes are filtered out. The remaining parcels preferentially entrain at higher altitudes where the environmental θ_e is lower. As a result, the updrafts' θ_e sampled at Z_{sample} decreases. This is why in figure 2-4c the composite θ_e decreases in regions with significant decreases in mass flux. This preference for parcels that entrain at higher altitudes also contribute to the smaller w decrease in the lower-left part of figure 2-3b,e. This is because these parcels enjoy undiluted buoyancy acceleration over a longer distance, thus attain higher kinetic energy. While parcels that entrain at higher altitudes also lose more kinetic energy because they have greater w at the time of entrainment, this effect is weaker compared to the buoyancy effect. Thus the preferential elimination processes described above have the effect of increasing the composite updrafts' w. This effect is most significant where there is substantial fractional mass flux decrease. Our analysis shows that in the region with fractional mass flux decreases over 60%, this elimination process has an effect on w that is nearly equal to the effect of additional buoyancy gained by entraining warmer environmental air.

The above analysis is only for parcels with one set of initial conditions and purity. One can do similar calculations for parcels with different initial conditions and purities. If the temperature perturbation can effectively lift the critical height, then it will decrease the mass flux and θ_e of the composite updrafts reaching Z_{sample}. It will also partially compensate for the slowdown of the composite updrafts reaching Z_{sample} due to the decrease in the height-integrated buoyancy.

2.3.3 Responses in the T1262 case

We have performed the same analyses as in the previous subsection for the T1262 case. While for the T987 case, we ran the simulation for 3 hours to provide a sense of longer time evolution of the anomalies, because of limited computational resource, we ran the T1262 case and the Q987 case described in the next subsection only for 1 hour, which is the period over which we sample the statistics of the cloudy updrafts.

The evolution of the large-scale environment is shown in figure 2-7. Its responses are generally similar to the T987 case: strong local cooling, moistening below and drying above the perturbation. The responses of the distributions of cloudy updraft properties and the comparison between the LES and the SPM (figure 2-8) also share many similarities with the T987 case, which indicates that the mechanisms discussed in the T987 case also operate in the T1262 case. The main difference between these two cases is that the decay of the initially imposed anomaly is slower in the T1262 case than in the T987 case. Because the fractional changes in mass flux are similar in the T987 and T1262 cases, it is presumed here that the different decay rates are because the background (control run) liquid potential temperature θ_l flux convergence at 1262-5m is smaller than at 987.5m so that changes in the θ_l flux convergence caused by the temperature perturbation at 1262.5m are also smaller than at 987.5m. On the other hand, the background q_t flux convergence at 1262.5m is of a similar magnitude as that at 987.5m, so the moisture responses in the T1262 case (figure 2-7b) is comparable to that in the T987 case (figure 2-1c).

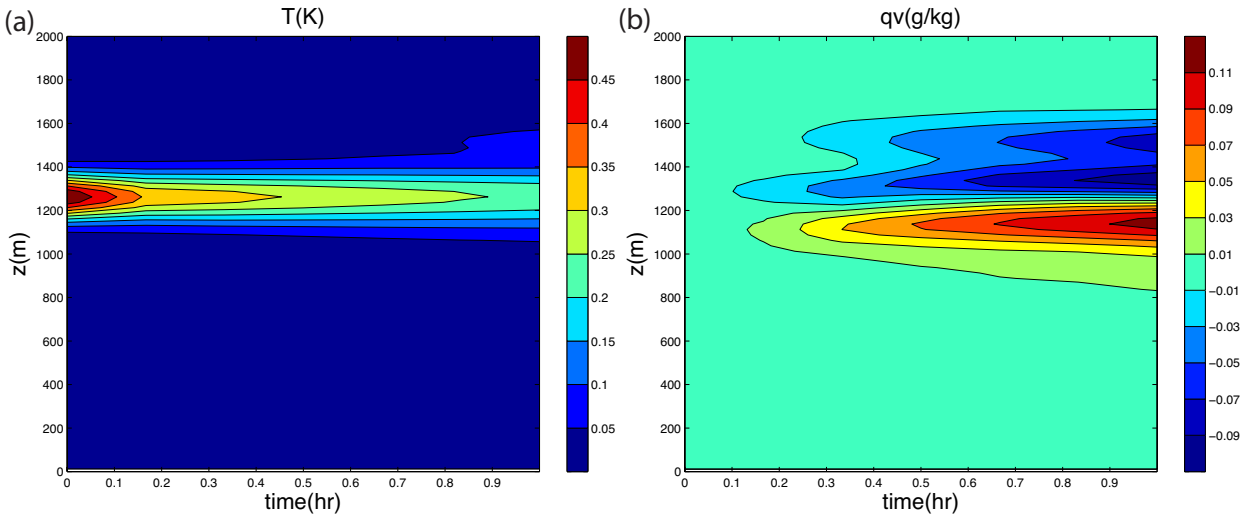

Figure 2-7: Same as figure 2-1b and c, but for the T1262 case. Note it only shows evolution of the soundings over the first hour after the perturbation is added.

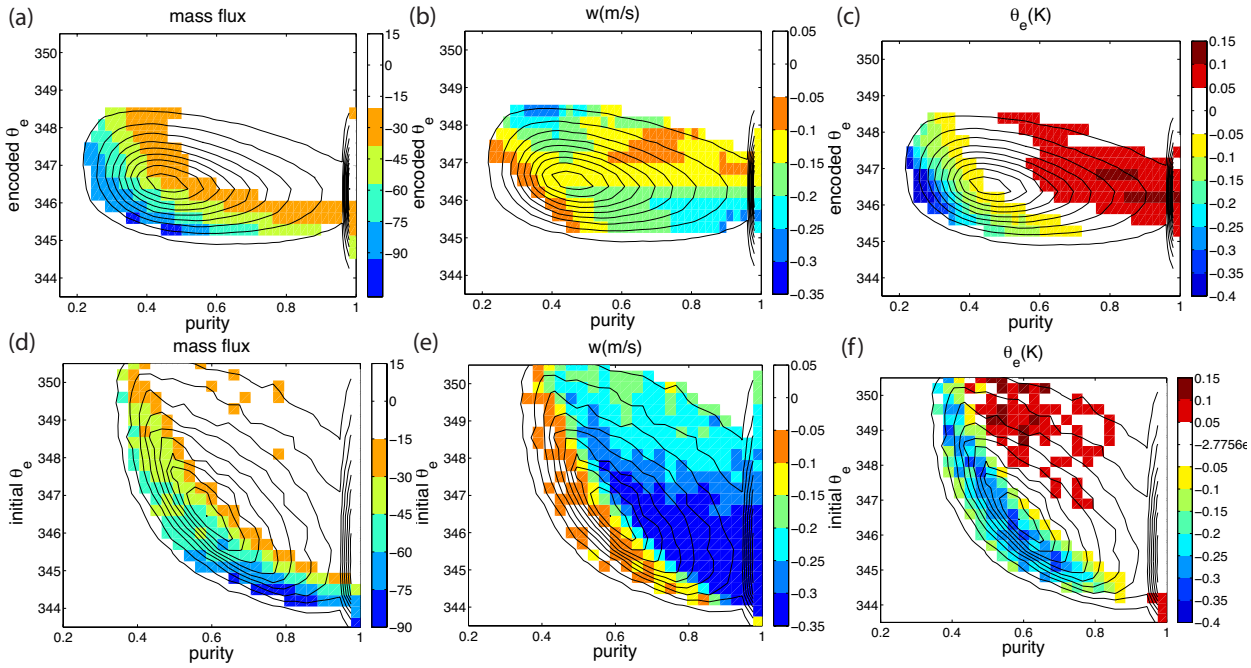

Figure 2-8: Same as figure 2-3, but for the T1262 case.

2.3.4 Responses in the Q987 case

The responses to moisture perturbations are quite different from those to temperature perturbations. The added moisture anomaly is also damped as expected (figure 2-9b). However, the temperature responses are remarkably small, of the order of 10^{-3}. Note that we have corrected for the effect of the hydrostatic adjustment (which produces a negative temperature anomaly with a peak amplitude of $9.5\times10^{-3}\ K$ and the same shape as the added moisture anomaly) as discussed in Section 2.2.2. The temperature in the perturbed layer increases with time, while there is cooling centered around 1500m in the inversion layer. These changes are consistent with an enhancement of cloudy updrafts by the added moisture anomaly, which warms the perturbed layer and causes the cooling near 1500m through penetrative entrainment in the inversion layer.

Statistics of cloudy updrafts again show general agreement between the LES and the SPM (figure 2-10). Both LES and SPM show that mass flux in the low purity and low $\theta_{e,ed}$ region increases while mass flux in the other regions is mostly unchanged. It indicates that a more moist environment benefits less buoyant updrafts by increasing their θ_e. The w distribution of the SPM shows an increase over a tilted band with purity around 0.5. Over the area with purity close to 1, w is decreased because the moisture perturbation increases environmental buoyancy slightly, which decreased height-integrated buoyancy (or potential energy) available to undiluted parcels. The w signal of the LES is relatively noisy. It also shows increases in the region with medium purity values, similar to that of the SPM. There is also a hint of w increase near purity of ~0.8, which is not captured by the SPM. The w increase in the region with medium purity values is because of the entrainment of higher θ_e air, which boosts the parcel/updraft buoyancy and increases its vertical velocity. This effect is significant only for parcels/updrafts that

experience significant entrainment. For parcels that entrain too heavily (i.e. those with the lowest purity values), however, the same effect of entrainment height selection discussed in Section 2.3.2 comes into play: with a positive moisture perturbation to the environment, parcels/updrafts that entrain at lower altitudes and could not reach the sampling height can now reach it. These parcels have had undiluted buoyancy acceleration over shorter distances and thus lower vertical velocities, weighting down the average w of parcels with low purities. For both LES and SPM, θ_e shows general increases over all the regions because the moisture anomaly increases environmental θ_e. For updrafts with lower purity, the increase in θ_e is larger because these are parcels that entrain more.

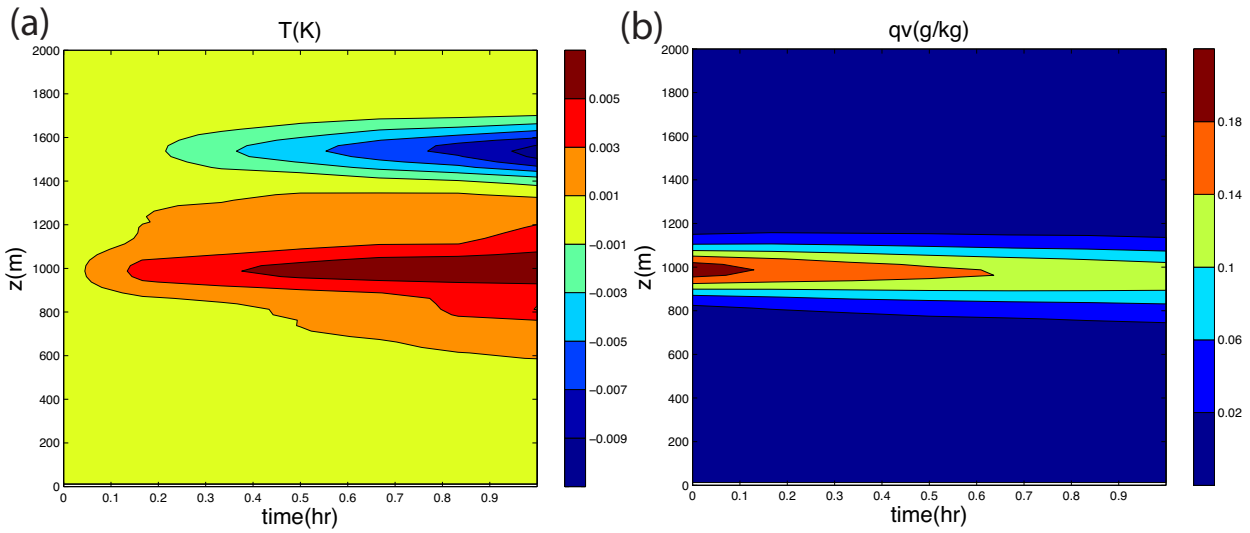

Figure 2-9: Same as figure 2-1b and c, but for the Q987 case. Note it only shows evolution of the soundings over the first hour after the perturbation is added.

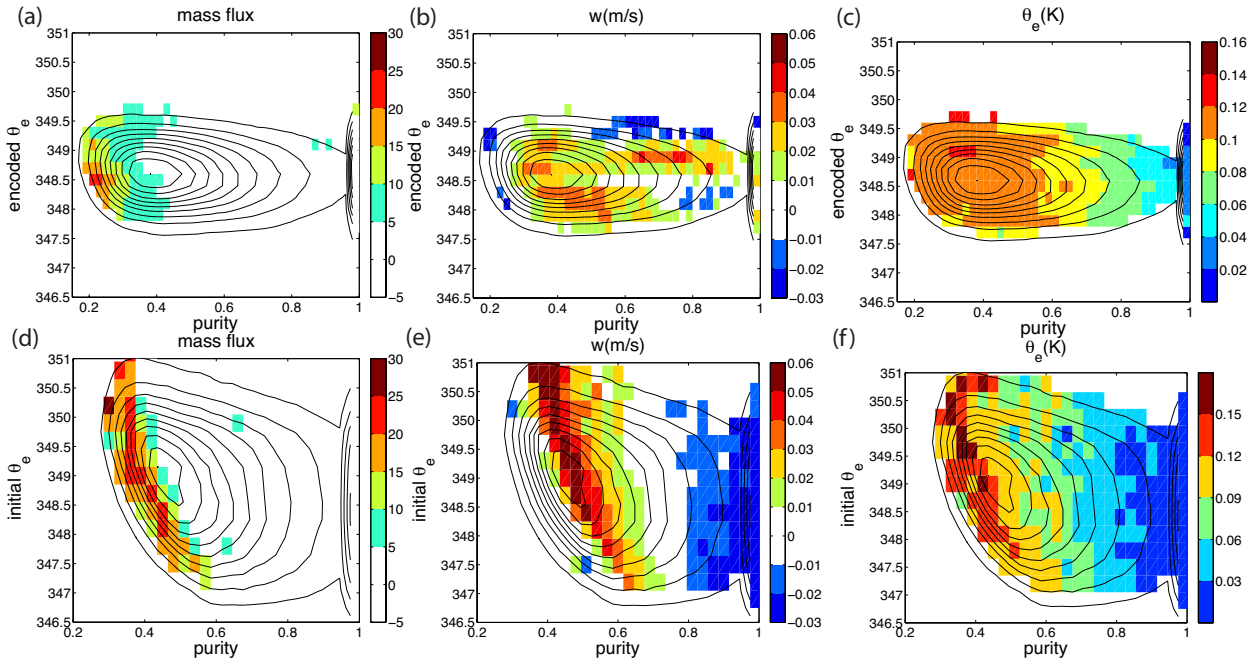

Figure 2-10: Same as figure 2-3, but for the Q987 case.

The reason that responses in mass flux and heating are very small for the moisture perturbation is that moisture anomalies are inefficient in changing either the environmental air's or the updrafts' buoyancy. Note that a 0.2g/kg specific humidity change in similar to a 0.5K temperature in terms of the change to the equivalent potential temperature. To illustrate this point, we plot the mixing diagrams (as in e.g. Bretherton *et al*. 2004) of a typical parcel with environmental soundings of the control, T987 and Q987 cases at the 987.5m height (figure 2-11). The parcel has $T = 293.67\ K$, $q_t = 16.82\ g\ kg^{-1}$ at $Z_{release} = 762.5\ m$, and is taken to rise undiluted to 987.5m then mix with the environment. With the temperature anomaly, the environmental density decreases significantly so that almost all mixtures are negatively buoyant. However, differences between the mixing lines of the control and Q987 cases are very small. The environmental density is decreased slightly with the moisture anomaly, shown as the slight descent of non-mixed points with $\chi = 0$ (χ is the fraction of environmental air in the mixture). The χ value corresponding to neutral buoyancy only shifts rightward slightly with the moisture anomaly. When normalized by their contributions to moist static energy anomalies, moisture anomalies are not efficient in changing updrafts' fate in the BOMEX case, compared to temperature anomalies.

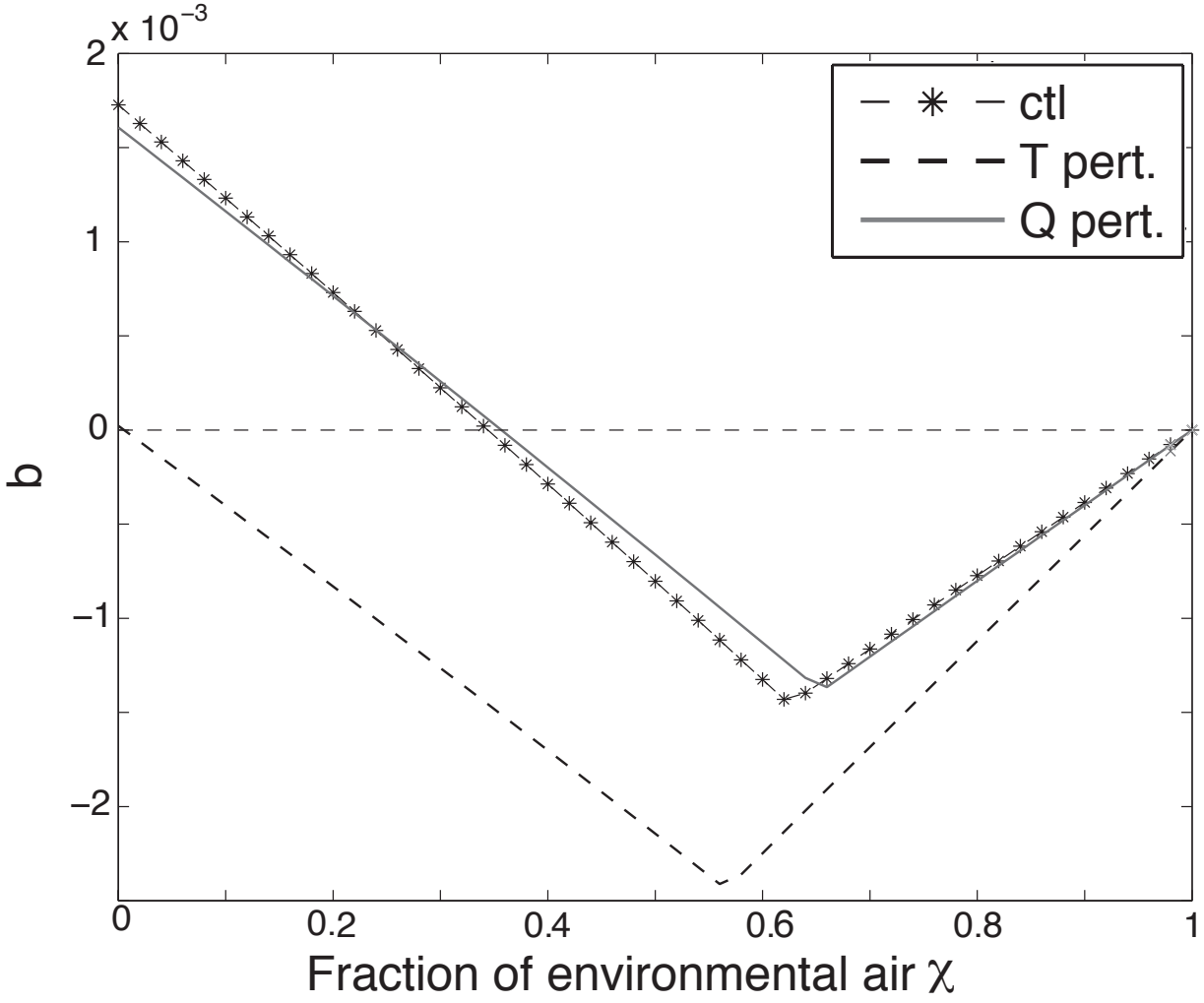

Figure 2-11: Buoyancies, divided by gravitational acceleration, (i.e. minus of the fractional density anomaly or b) of a typical cloudy updraft parcel after mixing different fractions (χ) of environmental air at 987.5m. A value of b greater than 0 indicates positive buoyancy. The dot-dash line uses the environmental sounding from the control runs, while the dash line uses the T987 sounding and the solid line uses the Q987 sounding.

2.4 Conclusions

In this chapter, the responses of a shallow cumulus ensemble to large-scale temperature and moisture perturbations are investigated using an LES and a stochastic parcel model. The main findings are:

1. The SPM in general reproduces the LES responses to large-scale temperature and moisture perturbations, not only in terms of the domain mean heating and moistening tendencies, but also in terms of changes in the statistics of the cloudy updrafts. The stochastic entrainment scheme in the SPM is key for the SPM to match the LES results. It suggests that the stochastic entrainment approach is a good way of representing the mixing process in simple models.

2. There are however some discrepancies in the w field between the SPM and LES responses, suggesting the treatment of momentum evolution in the SPM might be overly simplistic.

3. A positive temperature perturbation to the environmental sounding forms a buoyancy barrier that inhibits cloudy updrafts that have lower initial θ_e or entrain heavily.

4. For parcels that have the same amount of entrainment, the height at which parcels entrain is important in deciding their fate. Parcels entraining at higher altitudes are more likely to survive the buoyancy barrier and vice versa.

5. Convective heating responses to moisture perturbation above the cloud base are quite small for a shallow cumulus regime like BOMEX.

CHAPTER 3

A SHALLOW CONVECTIVE PARAMETERIZATION BASED ON STOCHASTICALLY ENTRAINING PARCELS

In Chapter 2, the SPM shows general success in reproducing the control state and responses of cloudy updrafts' statistics to large-scale temperature and moisture perturbations. In this chapter, we develop the SPM further into a parameterization of shallow cumulus convection. Air parcels are released from the surface layer and temperature/moisture fluxes carried by the parcels are used to calculate heating/moistening tendencies. Initial results show that this conceptually simple parameterization produces realistic convective tendencies and also reproduces the LES-simulated mean and variance of cloudy updraft properties. To examine the responses of convection to temperature/moisture perturbations in this parameterization, its LRF matrices are calculated. The evolution of initially introduced temperature and moisture anomalies predicted by the LRF matrices of the parameterization general matches the LES simulations, which further confirms the results in the previous chapter and the validity of the parameterization.

3.1 Introduction

The basic function of a convective parameterization is to use large-scale variables to estimate tendencies of mass, heat, moisture, momentum and other tracers due to convective motions.

A moist convective parameterization typically contains the following two key components:

The first is the determination of cloud base conditions. The second is a cloud model that describes the evolution of clouds as they rise above the cloud base, a key being their interactions with the environmental air.

A variety of approaches have been used for the cloud model, including, for example, a bulk constant entrainment plume or an ensemble of plumes with fixed entrainment rates (e.g. Simpson 1971, Arakawa and Schubert 1974, Tiedtke 1989, Bechtold *et al.* 2001). Some parameterizations include some coupling between entrainment and updrafts, an example being the buoyancy sorting approach (Raymond and Blyth 1986, Kain and Fritsch 1990, Bretherton *et al.* 2004). The stochastic entrainment method used in this chapter provides another approach to represent the mixing processes. This method explicitly simulates the stochastic nature of mixing, specified through the two probability distribution functions (equation (2.1) and (2.2)) described earlier in Section 2.2.

The determination of the cloud base conditions is what we need to extend the SPM into a parameterization. We shall follow a treatment similar to Cheinet (2003) and represent convective transport in the subcloud layer and that in the cloud layer within a single and unified framework. By doing so, we are assuming that fluxes in the subcloud layer are dominated by surface generated eddies and the subcloud layer turbulent fluxes can also be parameterized by the stochastic parcel model.

We will introduce the parameterization framework. Next we present simulation results from the parameterization and compare them with the LES results, including the responses to temperature and moisture perturbations. The main conclusions are then summarized and discussed in the last section of this chapter.

3.2 Constructing the parameterization scheme

We shall release parcels directly from the near surface layer (the lowest model level Z_s). The statistical distributions of these parcels' initial conditions (m, T, q_v, w at Z_s), where m is the mass of the parcel, will be determined by the surface fluxes (sensible heat flux F_H and latent heat flux F_L with a unit of $w\,m^{-2}$) and surface layer statistics. The treatment follows closely that of Cheinet (2003) and is described below for completeness.

Variations in T, q_v, and w near the surface are approximated by Gaussian distributions. In addition, both measurements and LES diagnostics show that near the surface, w, T and q_v are strongly correlated with each other. Let C_{xy} be the correlation coefficient between X and Y. We shall treat C_{wT}, C_{wq}, C_{Tq} as given parameters.

First, we assume that w follows a Gaussian distribution s with a zero mean and a standard deviation of σ_w:

$$s = \frac{1}{\sqrt{2\pi}} \exp(-\frac{w^2}{2\sigma_w^2}), \tag{3.1}$$

where σ_w is specified using the formula (A3, A4) in the appendix of Cheinet (2003):

$$\sigma_w = 1.9(\kappa g Z_s \frac{F_H}{\overline{T} c_{pa}})^{1/3}, \tag{3.2}$$

and $\kappa = 0.4$ is the von Karman constant, c_{pa} is the dry air heat capacity at constant pressure, $\overline{T}$ is the mean environmental temperature at Z_s, g is the gravitational acceleration.

We now describe how to infer distributions of T from the surface sensible heat flux. We shall describe T as

$$T = \overline{T} + \frac{\sigma_T}{\sigma_w} C_{wT} + x \,, \tag{3.3}$$

where σ_T is the standard deviation of temperature. x represents a white noise and is independent of w with a standard deviation of σ_x. From the definition of σ_T and C_{wT}, we have

$$\sigma_T^2 = C_{wT}^2 \sigma_T^2 + \sigma_x^2 \,, \tag{3.4}$$

$$\sigma_w \sigma_T C_{wT} = \int w(T - \overline{T}) s dw = \frac{F_H}{\overline{\rho} c_{pa}} \,. \tag{3.5}$$

In the above equation, the density of each parcel is approximated by the environmental mean density $\overline{\rho}$ in calculating F_H. The same approximation is applied later in equation (3.8). Given surface sensible heat flux F_H, σ_T and σ_x can be calculated from equations (3.4) and (3.5).

The procedure to infer distributions of q_v is similar to that of T. We shall describe q_v as

$$q_v = \overline{q_v} + \frac{\sigma_q}{\sigma_w} C_{wq} + \frac{\sigma_q}{\sigma_x} C_{xq} x + y \,, \tag{3.6}$$

where $\overline{q_v}$ is the mean environmental specific humidity. σ_q is the standard deviation of q_v. y is a white noise independent of both w and x. In addition, from the definition of σ_q and C_{wq}, we have

$$\sigma_T^2 = C_{wT}^2 \sigma_T^2 + \sigma_x^2 \,, \tag{3.7}$$

$$\sigma_w \sigma_T C_{wT} = \int w(T - \overline{T}) s dw = \frac{F_H}{\overline{\rho} c_{pa}} \,, \tag{3.8}$$

where L is the latent heat of vaporization. From equations (3.3) and (3.6), we have

$$C_{qT} = C_{wT} C_{wq} + \frac{C_{xq} \sigma_x}{\sigma_T} \,, \tag{3.9}$$

σ_q , σ_y and C_{xq} can then be solved from equations (3.7) to equation (3.9). As a summary, given inputs F_H, F_L and parameters σ_w, C_{wT}, C_{wq}, C_{Tq}, the statistic distributions of the initial conditions are determined.

In the parameterization, w is discretized into N_1 bins between 0 and $\alpha\sigma_w$ (we use a $\alpha = 3$, and the truncated tail is sufficiently small):

$$w_i = \frac{i\alpha\sigma_w}{N_1}, \quad i = 1,...,N, \tag{3.10}$$

$$s_i = \frac{1}{\sqrt{2\pi}N_1}\exp(-\frac{(i\alpha)^2}{2N_1^2}). \tag{3.11}$$

s_i can also be viewed as the fractional area occupied by the parcels belonging to the i th bin. The mass of parcels in the i th bin that cross the lowest model level above the surface over area Π during Δt is

$$M_i = \rho \times velocity \times area \times time = \rho w_i s_i \Pi \Delta t. \tag{3.12}$$

We further divide the air mass of each bin into N_2 parcels equally. So the total number of parcels released is $N_1 \times N_2$ and the mass of each parcel is

$$m_i = \frac{\rho w_i s_i \Pi \Delta t}{N_2}. \tag{3.13}$$

The reason to divide each bin is because entrainment in this parameterization is a stochastic process. It requires the number of parcels to be large enough to ensure statistical stability. In the later derivation, we will find that the factor $\Pi\Delta t$ is cancelled in the calculation of convective tendencies.

In our method, because s_i decays exponentially as i^2 increases, the total mass of parcels with large w is much smaller than that of parcels with smaller w. By using the same N_2 for all

vertical velocity bins, the implied mass per parcel is much smaller for the high w bins. One could carefully divide the i th bin into $N_{2,i}$ parcels, so that each parcel has a mass that is close to the mass of air blobs in the real atmosphere (or the LES). However, in that case, we will find the number of low w parcels to be much larger than the number of high w parcels, and most of the computational resources will be spent on the low w parcels, which are less important in the convective mass flux calculation, instead of the high w parcels, which will be underrepresented given computational constraints. Furthermore, the implied mass per parcel is inconsequential in our scheme because drag force is ignored in this parameterization, so that the size of a parcel does not affect its evolution and the outputs of the parameterization. In other words, we set all $N_{2,i}$ to the same value for computational economy and do not suggest that there is certain relationship between the size of the parcel and its vertical velocity.

With the initial statistical distributions in place, parcels are drawn randomly from this distribution and released from the lowest model layer. These parcels will rise, mix with the environment, oscillate around their neutral buoyancy level, and eventually come to rest. The evolution history of the parcels are solved by integrating the prognostic equations of parcel properties, with the entrainment processes specified as in section 2a and in Romps and Kuang (2010a,b). Because the mixing processes in the subcloud layer are different from those in the cloud layer, a different set of entrainment parameters (λ, σ) are used in the subcloud layers, and tuned to give satisfactory results. Since we focus on shallow convection, precipitation and ice processes are turned off.

The temperature and moisture fluxes affected by the parcels are used to estimate the convective heating and moistening tendencies. Let the environmental soundings ($\theta_{l,en}$, $q_{t,en}$) be specified on discrete levels Z. (We choose θ_l as the prognostic temperature variable.) The fluxes are defined

on half levels Z_h. The transports (fluxes times area times time) carried by these parcels across a certain level can easily be obtained by summing over all parcels that cross this level:

$$mass\ \ transports = \sum m_k \ , \tag{3.14}$$

$$\theta_l\ \ transports = \sum m_k \theta_{l,k} \ , \tag{3.15}$$

$$q_t\ \ transports = \sum m_k q_{t,k} \ . \tag{3.16}$$

where k is the index of parcels that cross this level over a time interval Δt. For parcels crossing this level from above, their transports should be marked as negative.

When the parcels rise, the environmental air subsides to compensate for the mass transport by these parcels and ensures that there is no net mass accumulation. The subsiding air also transports heat and moisture:

$$compensating\ \ mass\ \ transports = -\sum m_k \ , \tag{3.17}$$

$$compensating\ \ \ \theta_l\ \ transports = \sum m_k \theta_{l,dn} \ , \tag{3.18}$$

$$compensating\ \ \ q_t\ \ transports = \sum m_k q_{t,dn} \ . \tag{3.19}$$

where $\theta_{l,dn}$ and $q_{t,dn}$ are the mean θ_l and q_t for the compensating subsidence. Here we approximate the properties of the compensating subsidence by its mean values, thus neglecting transport due to variations within the compensating subsidence. This is a good approximation for the cloud layer (Siebesma and Cuijpers 1995), but is less accurate in the subcloud layer. Here $\theta_{l,dn}$ is estimated as

$$\theta_{l,dn} = \frac{\theta_{l,en} - \sum s_k \theta_{l,k}}{1 - \sum s_k} \ , \tag{3.20}$$

and the same for $q_{t,dn}$. The fractional area s_k occupied by a parcel at an interface averaged over a unit time is:

$$s_k = \frac{m_k}{\rho_k w_k \Pi \Delta t}. \tag{3.21}$$

The total fractional area occupied by convective updrafts ($\sum s_k$) is significant in the subcloud layer and negligible in the cloud layer.

The convective heating and moistening tendencies are the vertical convergence of the net fluxes (sum of the parcel transports and the compensating transports, then normalized by area Π and time period Δt) :

$$\frac{-\partial \theta_{l,en}}{\rho \partial t} = -\frac{\partial\left[\sum(m_k \theta_{l,k}) - \sum(m_k \theta_{l,dn})\right]}{\partial z}\frac{1}{\Pi \Delta t}, \tag{3.22}$$

$$\frac{-\partial q_{t,en}}{\rho \partial t} = -\frac{\partial\left[\sum(m_k q_{t,k}) - \sum(m_k q_{t,dn})\right]}{\partial z}\frac{1}{\Pi \Delta t}. \tag{3.24}$$

From Eq. (15), we see that area Π and the time interval Δt will be cancelled out in Eqs. (24) and (25).

3.3 The BOMEX run

We test the parameterization by running it in the BOMEX setting. The BOMEX initial soundings, large-scale forcing and surface fluxes for the parameterization run are the same as Siebesma and Cuijpers (1995). The vertical levels are from 80m to 3000m with a spacing of 160m. The environmental soundings are adjusted every $\Delta t = 60\ s$. The time integration scheme of equation (3.22-3.23) is forward Euler. The fluxes (3.15-3.16) are calculated by sampling the properties of parcels at half levels. When calculating the compensating fluxes (3.18-3.19), the minmod flux limiter scheme (Durran 1999) is used. The parameterization is integrated for 3 hours.

Parameters for the surface initial conditions are $C_{wT} = 0.58$, $C_{qT} = 0.55$ (which are the same as Cheinet (2003) and Stull (1988), although we use T instead of θ_v in these correlation coefficients), and $C_{wq} = 0.63$ (which comes from our LES diagnoses). We find that the parameterization results are not sensitive to those correlation coefficients over a large range. By setting $N_1 = 15$, $N_2 = 10$, the output is already statistically steady. Runs with much larger N_1 and N_2 do not alter the results.

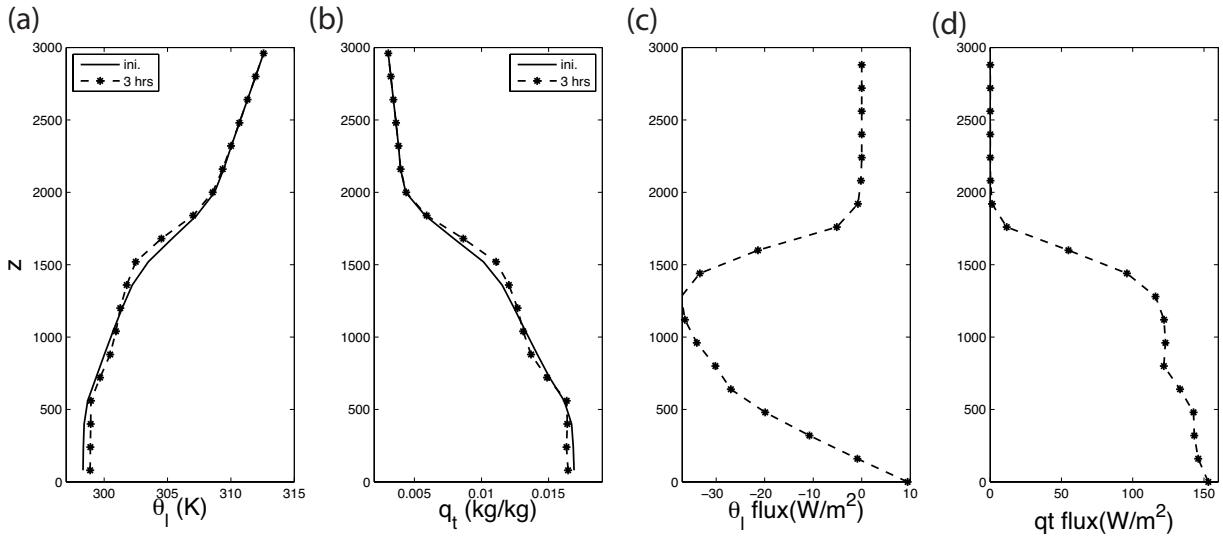

Figure 3-1: (a) The initial θ_l profile (solid) and the profile after a 3 hours parameterization run (dot-dash). (b) is the same as (a) but for the q_t profile. (c) the parameterization generated θ_l flux averaged between 1.5 to 3 hours of the parameterization run. (d) is the same as (c) but for the q_t flux.

We use the same entrainment parameters ($(\lambda = 125\,m, \sigma = 0.32)$ as described in Section 3.2. We find that the parameterization gives nearly equally good performance for large ranges of (λ, σ) along the bottom of the valley of the objective function in figure 7 of Romps and Kuang (2010a). Closer to the constant entrainment limit, however, the results degrade, and the intra-cloud variations (see later in figure 14) are severely underestimated. The cloud base is around 600m in the BOMEX case. For this first study, the subcloud layer entrainment parameters are specified as $(\lambda_{sbc} = 30\ m, \sigma_{sbc} = 0.06)$, which give fairly good results. In the future, efforts are needed to better constrain $(\lambda_{sbc},\ \sigma_{sbc})$.

The initial sounding and the sounding after 3 hours are shown in figure 3-1a,b. Although there are some drifts in the mean state, the convective tendency generally balances the large-scale forcing. The fluxes given by the parameterization (figure 3-1c,d) are broadly similar to the LES results (Siebesma and Cuijpers 1995, Cheinet 2004), except that our parameterization over-predicts both the negative θ_l flux and the positive q_t flux near 1300m.

We now sample the mean properties of "active cloudy air" for both the LES and the parameterization. Results using two definitions of "active cloudy air" are shown: one is cloudy updraft air as in Section 3.3 (parcels/grids with $q_l > 10^{-5}\ kg\ kg^{-1}$ and $w > 0.5\ m\ s^{-1}$), the other is cloud core with the same definition as Cheinet (2004) (parcels/grids with $q_l > 10^{-5}\ kg\ kg^{-1}$, $w > 0\ m\ s^{-1}$ and positively buoyant). The results show that the parameterization generally reproduces the results of LES with both definitions (figure 3-2). The exception is the cloud core w in the inversion. We have also examined the mean properties of cloudy air (saturated), or active cloud core with other definitions, the results all show agreement between the LES and the parameterization except for w in the inversion.

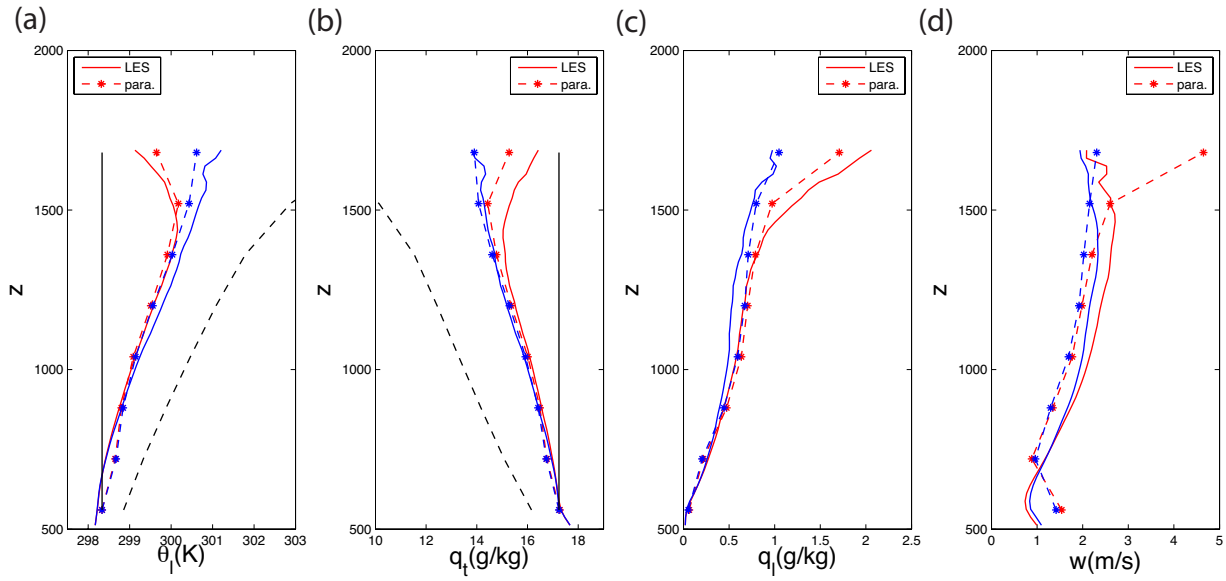

Figure 3-2: The mass flux weighed properties ((a) θ_l, (b) q_t, (c) q_l and (d) w) of cloudy updrafts. Solid lines are LES results and dot-dash lines are results from the parameterization. The blue curves are for cloudy updrafts, while the red curves are for the cloud cores. See text for definition. In (a) and (b), the black dash lines are the environmental profiles and the black solid lines are the adiabatic profiles from the cloud base.

Besides the mean values of these properties, the standard variations are also examined (figure 3-3). Once again, except layers that are in the inversion (above 1500m), the parameterization and the LES results match well. The discrepancy in w between the LES and the parameterization in the inversion layer is not fully understood and requires further investigation. One possible reason for the decrease in the LES simulated w could be enhanced wave drag. As parcels penetrate into the inversion layer, a region of strong stratification and thus higher buoyancy frequency, they can become more effective in exciting gravity waves and therefore become subject to enhanced gravity wave drag. Such processes are absent in the current parameterization. However, we note that Warren (1960) provided wave drag solutions that we can incorporate into our parameterization in the future.

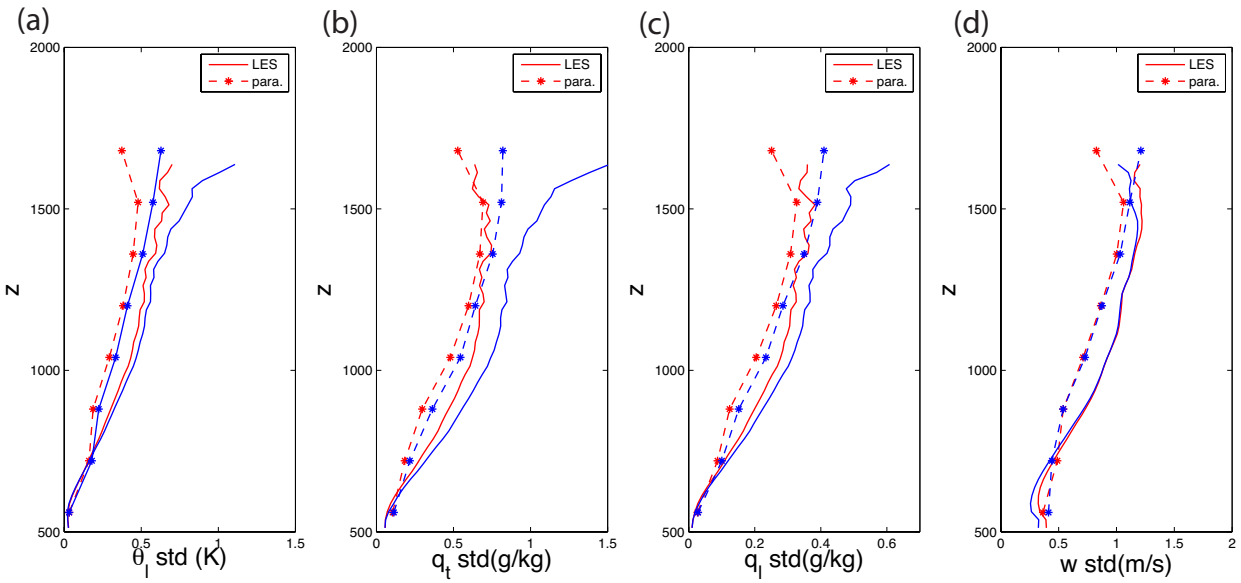

Figure 3-3: The standard deviation among modelled cloudy updrafts for (a) θ_l (b) q_t (c) q_l and (d) w. Solid lines are LES results and dot-dash lines are results from our parameterization. The blue curves are for cloudy updrafts, while the red curves are for the cloud cores.

3.4 Response of the parameterization to temperature and moisture perturbations

Another important aspect of the parameterization is to capture the response of convection to changes in the large-scale environment. To this end, we have computed the LRF matrix of this parameterization to a full set of temperature and moisture perturbations (using equation (1.6)). The LRF matrix of the parameterization is calculated by simply adding, one at a time, temperature/moisture anomalies in each layer of the mean sounding. The anomalous heating and moistening tendencies from the parameterization form the LRF matrix.

A comparison of the full LRF matrices from the parameterization and from the LES will be reported in a separate document. Here we shall only discuss the three perturbed cases (T987, T1262, Q987) described in Section 2.3.

The time evolution of the sounding anomalies for the T987, T1262, and Q987 cases are shown in figure 3-4, and should be compared with LES results shown in figure 2-1, figure 2-7 and figure 2-9. Note that results in figure 3-4 are for an integration over 3 hours. The agreement is quite good in terms of both the pattern and the magnitudes of the responses. The warming seen in the parameterization in response to the moisture perturbation however, appears stronger than that in the LES.

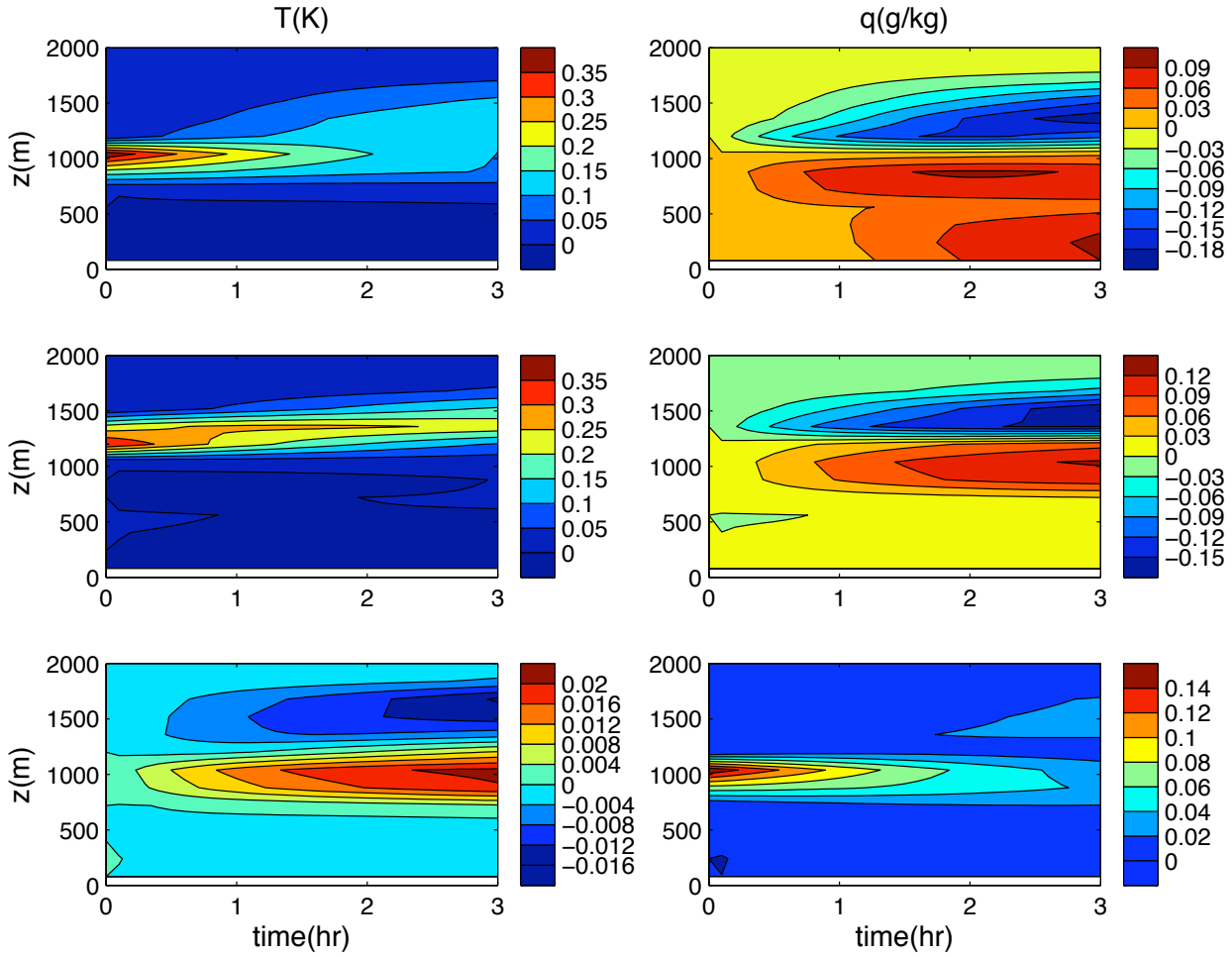

Figure 3-4: Evolutions of (left column) temperature and (right column) moisture anomalies after the initial perturbation is introduced as simulated using the linear response functions of the parameterization. The first, second and third rows are for the T987, T1262, and Q987 cases, respectively.

3.5 Conclusions and Discussions

In this chapter, we have further introduced a parameterization of shallow cumulus convection (including subcloud layer turbulence) based on the stochastic parcel model. The parameterization differs from the previous parameterizations based on bulk entraining/detraining plume models (e.g. Yanai *et al.* 1973, Kain and Fritsch 1990, Bechtold *et al.* 2001, Bretherton *et al.* 2004) or ensemble plume/parcel models (Arakawa and Schubert 1974, Neggers and Siebesma 2002, Cheinet 2003), but is closer in spirit to episodic mixing models of Raymond and Blyth (1986) and Emanuel (1991). The parameterization gives promising results in terms of both the simulated mean state and the simulated responses to temperature and moisture perturbations.

We argue that an important advantage of the SPM and the parameterization based on it is that they explicitly include the inhomogeneity of cloudy air associated with the stochastic mixing process. Although other ensemble plume/parcel model also contains some inhomogeneity of cloudy air at the same height, the inhomogeneity is only introduced through variations in the cloud base conditions (e.g. Neggers *et al.* 2002). The present approach includes the variations introduced by the stochastic nature of mixing, which was shown to be the main cause of inhomogeneity in cloudy air (Romps and Kuang 2010). Capturing this inhomogeneity is important in order to better simulate microphysics and chemistry beyond the goal of simulating the heating and moistening tendencies. Compared to the assumed PDF approach (e.g. Lappen and Randall 2001, Larson *et al.* 2002, Golaz *et al.* 2002), the present approach may be viewed as a Monte-Carlo version of the PDF approach; while it is somewhat more expensive, it can be more general and versatile in dealing with different PDFs. We note that cost-saving with this parameterization may be achieved using the approach of Pincus *et al.* 2003), where one

subsamples the PDFs at each time step but builds up sufficient sampling over many time steps of the model integration.

Certain treatments in the present parameterization are chosen for simplicity and could and should be improved in the future. For example, the current neglect of momentum drag on the parcels, including the lack of wave drag, is clearly unrealistic. Notwithstanding the need to balance simplicity and realism, effects of gravity wave drag as described in Warren (1960) should be explored. The lack of inter-parcel interaction is also an idealization based on a limiting scenario, bulk plume being the opposite extreme of instant inter-parcel homogenization. In-cloud mixing of parcels and/or momentum exchanges without actual mixing of parcels could be added in the spirit of Krueger *et al*. (1997). We have limited ourselves to shallow non-precipitation cumuli in the current parameterization and have neglected precipitation processes. How to extend the current model to include the additional processes brought about by precipitation so that it can serve as a unified parameterization for both shallow and deep convection is a research question for future studies.

CHAPTER 4

A NEW FRAMEWORK FOR DIAGNOSING MIXING IN CUMULUS CONVECTION

A new framework for diagnosing mixing in cumulus convection is proposed, where the vertical evolution of the cloud mass flux distribution as a function of given parcel properties is viewed as a mapping process. Matrices that characterize this mapping process are constructed using a Lagrangian particle dispersion model embedded in a LES. Extending previous use of LES-diagnosed bulk entrainment and detrainment rates to test bulk plume models, the construction of these mapping matrices from LES provides a reference, against which multiple-parcel models can be compared. The framework is further applied to diagnose the response of shallow cumuli to a small temperature perturbation.

4.1 Introduction

Despite the success of bulk entraining/detraining plume models (e.g. Siebesma and Cuijpers 1995, Bretherton *et al.* 2004) in reproducing the domain averaged heating and moistening rates of shallow cumulus convection, there have been increasing efforts on multiple-parcel/plume models (e.g. Emanuel 1991, Neggers *et al.* 2002, Cheinet 2004, Nie and Kuang 2012a). The multiple-parcel/plume models (simply called multi-parcel models hereafter) can potentially account for in-cloud turbulent fluxes. More importantly, they naturally predict the variability of cloudy updrafts. Representing the heterogeneity within the updrafts can be important for microphysics and chemistry, which involve highly non-linear reactions or microphysical processes. Thus, the multi-parcel models are more versatile and can be a useful extension of the bulk plume models.

A key aspect of the multi-parcel models is the representation of turbulent mixing among cloudy updrafts and between cloudy updrafts and their environment. Detailed numerical simulations such as LES can potentially be used to constrain such representations, provided that the LES results are diagnosed properly in the framework of a given conceptual model or parameterization scheme. In the framework of a bulk plume model, such turbulent mixing is characterized by the bulk entrainment/detrainment rates, and Siebesma and Cuijpers (1995) pioneered an analysis of LES results to evaluate entrainment/detrainment rates used in bulk plume models. Here, we propose a diagnostic framework that extends the analysis of Siebesma and Cuijpers (1995) to multi-parcel models. After introducing our framework, we will apply it to a shallow convection case and compare the results to those from two multi-parcel models. We will then apply it to probe the response of shallow convection to a large-scale temperature anomaly (Kuang 2010, Tulich and Mapes 2010, Nie and Kuang 2012a).

4.2 The Mapping Diagnostic Framework

We shall assume that transports by cloudy updrafts and the corresponding environmental subsidence dominate the total convective transports, which is reasonable for shallow cumulus convection (Siebesma and Cuijpers 1995). We define cloudy updrafts as grids with liquid water content greater than 0.01 $g\,kg^{-1}$ and vertical velocity w greater than 1 $m\,s^{-1}$. Conclusions here are not sensitive to this definition. The cloudy updraft mass flux can be binned on a given parcel property ϕ (such as total water q_t or liquid water potential temperature θ_l as a distribution function $m(\phi)$. With the assumption that the environment is homogenous, the total convective flux of ϕ is

$$F(\phi) = \int m(\phi)(\phi - \phi_{env})\,d\phi\,, \tag{4.1}$$

where ϕ_{env} is the environmental ϕ. Instead of assuming a uniform ϕ in cloudy updrafts as in bulk plume models, the mass flux distribution $m(\phi)$ provides a characterization of the in-cloud variations of ϕ. The environment is assumed to be homogeneous here to simplify the analysis. The mapping framework is sufficiently general, if needed, to account for heterogeneity in the environment as well.

We shall view the evolution of $m(\phi)$ with height as a mapping process. From a level n to level n+1, the function that maps $m_n(\phi)$ onto $m_{n+1}(\phi')$ (Prime indicates the higher level.) describes the result of turbulent mixing of cloudy updrafts and the environment from the perspective of property ϕ.

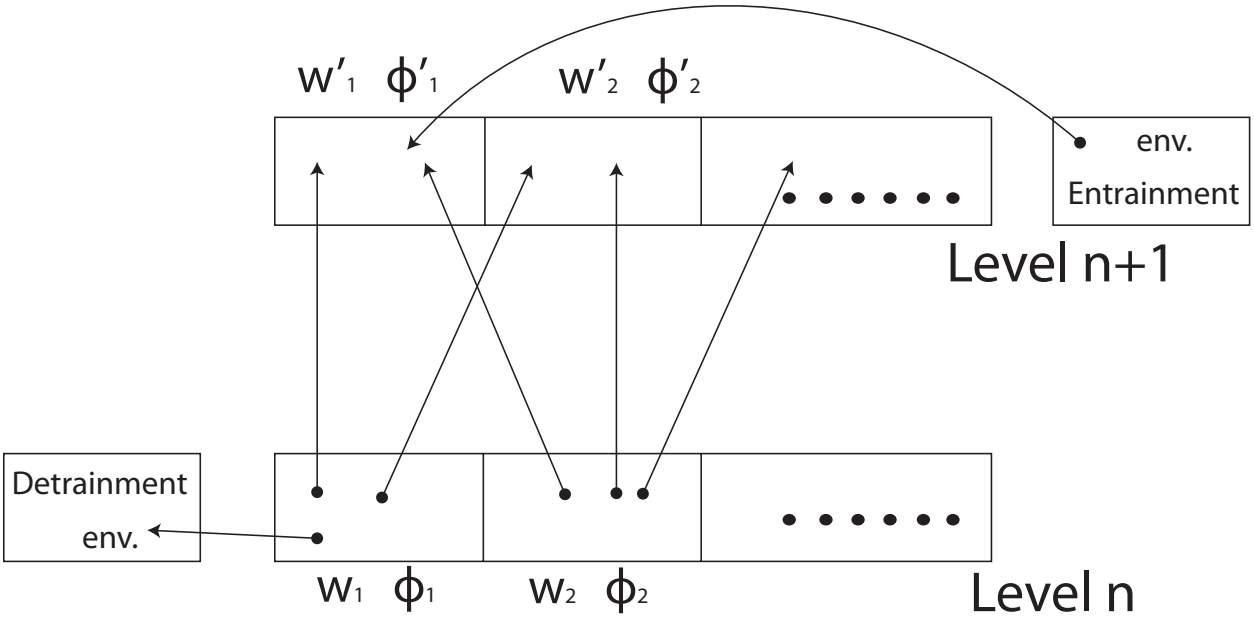

Figure 4-1: A diagram of the mapping process. See text for details.

Next we introduce how to construct the mapping function in a discretized form using the LPDM (Lagrangian particle dispersion model, see Section 1.3.3 for introduction of LPDM) (Weil *et al.* 2004). Figure 4-1 is a diagram of the process, where each box represents a cloudy updraft grid and each arrow represents a trajectory of a Lagrangian particle that links two grids at different heights. Starting from a grid, there are N Lagrangian particles (in the diagram, 3 particles are plotted as an illustration.) that are advected by LES winds and are dispersed with time. It is assumed that each particle represents $1/N$ of the grid's mass. For a cloudy updraft, for example, grid '1', a subset of the particles may leave the cloud and enter the environment, which represents the detrained mass flux. We bin these particles on ϕ to define a diagonal matrix $D(\phi,\phi)$ that describes the fractional detrainment rate per unit mass flux as a function of ϕ. For the particles that rise to level n+1 inside a cloud, due to turbulent mixing, the trajectories are dispersed to different grids, for example, grids with ϕ_1' and ϕ_2'. Each of these trajectories connects some portion of the mass flux with certain ϕ at level n and some portion of the mass flux with certain ϕ' at level n+1. These trajectories are binned into the mapping matrix $A(\phi',\phi)$ and normalized by the non-detrained mass flux. For a grid at level n+1, not all of its particles can be tracked back to cloudy updrafts at level n. Some are entrained from the environment. Similar to $D(\phi,\phi)$, a diagonal entrainment rate matrix $E(\phi',\phi')$ is defined as the ratio of the entrained mass flux to the non-entrained mass flux.

Since we are interested in the local mixing processes as cloudy updrafts move from one level to another level, we track each particle only within the time interval between $t_0-\tau$ and $t_0+\tau$, where t_0 is the time the particle crosses from level n to level n+1. For a vertical spacing of 50m used in this study (Section 4.3), we use a τ of 50 s, which is the time that the slowest updrafts (from our definition of $w \geq 1\, m\, s^{-1}$) take to traverse this vertical spacing. If a parcel leaves and

re-enters cloudy updrafts between $t_0 - \tau$ and $t_0 + \tau$, its departure and reentrance are not considered as detrainment and entrainment events. The results here are not sensitive for $\tau \in [40s, 100s]$.

We do the tracking for all particles in cloudy updrafts so that the mapping from $m_n(\phi)$ to $m_{n+1}(\phi')$ reads

$$m_{n+1}(\phi') = \left(I + E(\phi', \phi')\right) A(\phi', \phi) \left(I - D(\phi, \phi)\right) m_n(\phi), \tag{4.2}$$

where I is the identity matrix. In equation (4.2), the mapping process is naturally separated into three components with clear physical meaning; the detrainment rate matrix $D(\phi, \phi)$, the entrainment rate matrix $E(\phi', \phi')$ and matrix $A(\phi', \phi)$ that maps the non-detrained mass flux to the non-entrained mass flux. Equation (4.2) can be applied recursively over multiple levels. Knowing the mass flux distribution on one level (e.g. cloud base) and the mapping matrices upward from that level, the mass flux distributions on all levels above can be determined and so can the flux $F(\phi)$. We note that Kuang and Bretherton (2006) also binned mass flux in terms of moist static energy and examined how its distribution varies with height in the framework of Arakawa and Schubert (1974). Our analysis here, through the use of a LPDM, significantly extends that study in that bins at different heights are connected by actual LES flow trajectories, instead of a hypothesized entraining plume model.

The more conventional concepts of bulk entrainment and detrainment rates can be viewed as the mapping functions with only one bin for the cloudy updrafts and one bin for the environment, i.e. the top-hat approximation. In the context of such a bulk plume model, entrainment and detrainment rates obtained from tracking the movement of air masses across the cloud-environment interface (as in e.g. the work of Romps (2010) and Dawe and Austin (2011a, b) and

with the Lagrangian particles as done here and contemporaneously by Yeo and Romps (2012) cannot describe the exchange of thermodynamic properties and tracers between the two bins. This is simply because bins in the bulk plume model are too coarse and miss the significant heterogeneity within a bin: air entrained from the environment or detrained from the cloud does not have the mean properties of its originating bin. Here, we use bins that are fine enough so that heterogeneity within each bin is insignificant in terms of ϕ and variables that covary with ϕ. In this chapter, we use only one bin for the environment, but the mapping framework allows for multiple bins for the environment as well. Entrainment and detrainment rates obtained from tracking the movement of air masses (done here through the LPDM) can now describe the exchanges of ϕ (and other properties that are sufficiently uniform within each bin), because they are given as functions of ϕ. Therefore, the mapping functions provide a more complete description of the mixing process and are a useful extension to the bulk entrainment/detrainment rates of the bulk plume model.

To better understand and parameterize convection, it is valuable to examine how convection responds to changes in its large-scale environment. We shall focus on the response to small perturbations, for which the changes of mass flux distribution can be separated into four terms by applying the chain rule on equation (4.2);

$$\begin{aligned}\delta m_{n+1} = &\left(I+E\right)A\left(I-D\right)\delta m_n - \left(I+E\right)A\delta D m_n \\ &+\left(I+E\right)\delta A\left(I-D\right)m_n + \delta E A\left(I-D\right)m_n\end{aligned} \tag{4.3}$$

The first term is associated with δm_n, the inputs at level n, keeping the mapping matrices unchanged. We shall call it the inherited term. The second to the fourth terms are changes of the mass flux distribution due to changes in the detrainment rate $D(\phi,\phi)$, the mapping matrix $A(\phi',\phi)$, and the entrainment rate $E(\phi',\phi')$, respectively.

The coordinate ϕ need not be a single variable. Mapping functions for joint mass flux distributions in terms of multiple variables (e.g. q_t and w) can in principle be constructed as well. The vertical distance over which the mapping matrices are constructed can be coarser than the LES vertical resolution based on the problem of interest. While we focus on shallow convection in this chapter, the analysis framework is also applicable to deep convection.

4.3 Experiments Design

In this and next sections, we will apply the mapping framework to a case of shallow convection and its response to a small temperature perturbation. The case that we use is the BOMEX case (Holland and Rasmusson 1973). The forcing and other settings are the same as the intercomparison study of BOMEX described in Siebesma *et al.* (2003).

The numerical simulation is done with the System for Atmospheric Modeling (SAM) model in a domain of 6km (x) × 6 km (y) × 3km (z). The LPDM is similar to that in Weil *et al.* (2004) and Heus *et al.* (2008) except that subgrid diffusion is not included. Heus *et al.* (2008) showed that including subgrid diffusion has little impact on the particles in the cloud layer. Properties of a particle inside an LES grid are set to the grid values with no interpolation. Using linear interpolation, as in Weil *et al.* (2004) and Heus *et al.* (2008), has little effects on the results presented here. The two choices (no interpolation and linear interpolation) are consistent with first- and second-order advection, respectively, and are expected to bracket the actual order of SAM's advection. To better resolve the mixing process, we use a resolution of 25m in all directions, and release 2 Lagrangian particles in each grid. The LES output is coarsened to a resolution of 100m × 100m × 50m, so there are 64 particles in a coarsened grid, sufficient to generate robust statistics. To test the robustness of the results with respect to resolution and the number of particles, we performed the same analysis on simulations with a resolution of 100m × 100m × 50m with 64 or 27 particles released in each grid, and the results are similar to those reported here.

The model is run for 6 hours and the first 3 hours are discarded as spinup. Between hours 3 to 6, restarts are saved every 5 minutes. The model is run for half an hour with the embedded LPDM

turned on using these restarts with and without a temperature perturbation

$$\delta T = 0.25 \exp\left(-\frac{1}{2}\left(\frac{z-1025}{100} \right)^2 \right) \; K \,, \tag{4.4}$$

(shown in figure 4-3f) introduced. The results in the next section are averaged over 150 ensemble members and they are statistically robust.

We shall use q_t, which is conserved in shallow non-precipitating convection, as the coordinate. While θ_l is also conserved, the introduced temperature perturbation changes the environmental θ_l in the perturbed runs, which causes additional complications when θ_l is used as the coordinate.

4.4 Results

The control run mapping matrices from the 975 m height to the 1025 m height (chosen to be close to the center of the introduced perturbation) is shown in figure 4-2a. The lowest panel is the mass flux distribution at 975 m ($m_n(\phi)$ in equation (4.2)). The detrainment matrix D shows that about 10% to 30% of the mass flux is detrained over this 50m layer (about 2-6 per km, comparable to the values from Siebesma and Cuijpers (1995). The detrainment rate is greater at lower q_t, indicating that updrafts with lower q_t detrain more strongly. The color map shows the matrix A (we plot $\sqrt{A}$ instead of A for a better illustration), where each column indicates how one unit of non-detrained mass flux on level n with a certain value of q_t is distributed on level n+1 (in terms of q_t'). Without any mixing, nonzero values of A will lie on the 1-to-1 line, and the values will deviate from unity only because of vertical acceleration or deceleration. Mixing with environmental air decreases updrafts' q_t. As a result, the peak values of A are slightly below the 1-to-1 line. Besides mixing with the environment, in-cloud mixing among the cloudy updrafts homogenizes their properties, shrinking the range of q_t'. The regions that are above the 1-to-1 line are the results of in-cloud mixing. The entrainment rate E has the same trend as D, with values decreasing as q_t increases, as grids with large amounts of entrained air have lower q_t. Note that in figure 4-2, we plot $E/(I+E)$ which is the ratio of entrained air mass to the total mass after the entrainment, which, like values in D, is always less than 1. For the other layers not shown here, the general dependence of D and E on q_t is similar.

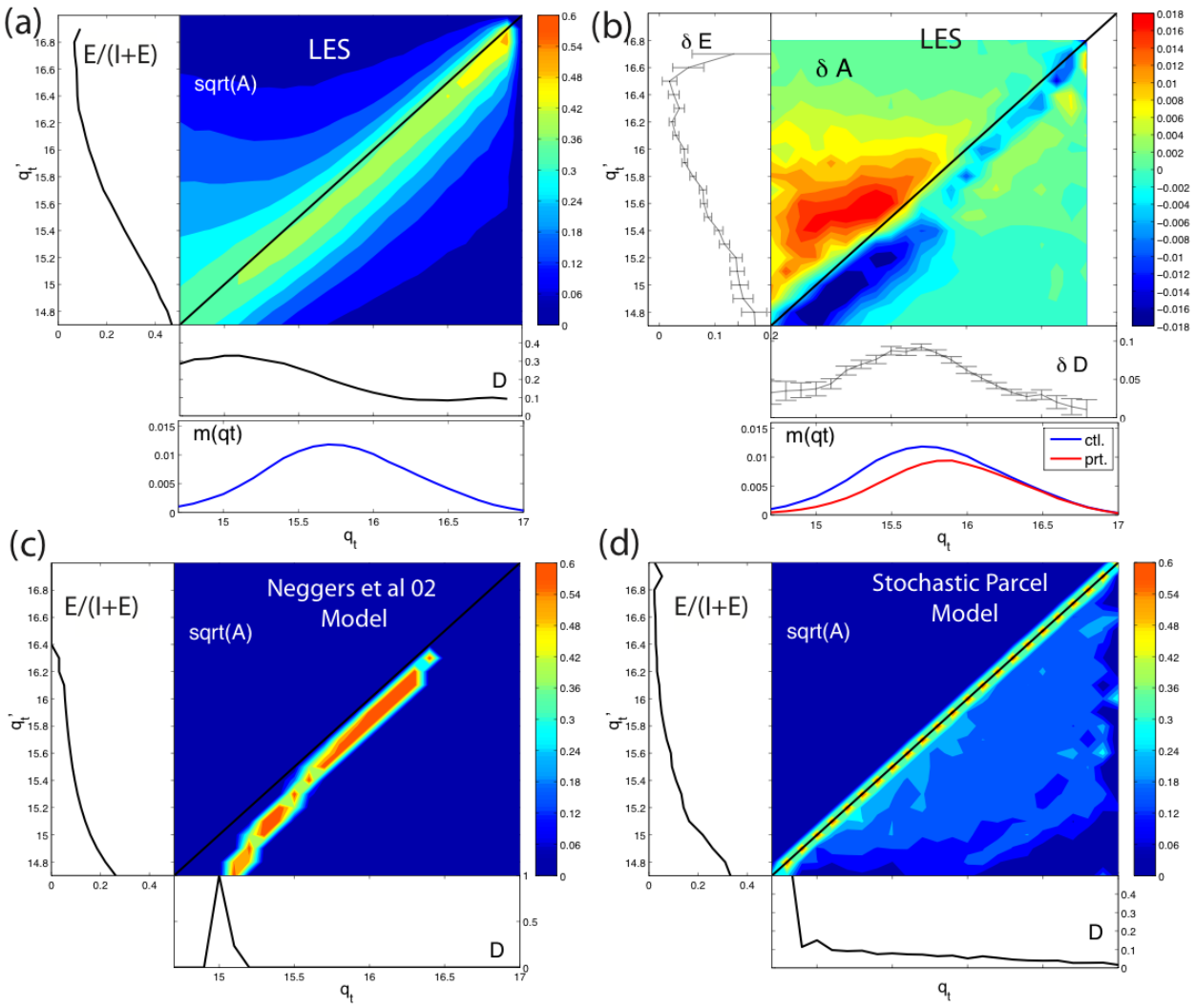

Figure 4-2: (a) The control run mapping matrices from 975 m to 1025 m using q_t as the coordinate. The lowest panel shows the distribution $m(q_t)$ at the 975 m level. The diagonal matrices $D(\phi,\phi)$ and $E/(I+E)$ are plot as function of q_t. The color map shows the matrix $\sqrt{A}$ (unitless) with the 1-to-1 line (black solid) superimposed. (b) is same as (a) but for the differences in the mapping matrices between the perturbed runs and the control runs. The color map shows δA. The error bars show the estimated uncertainties using the jackknife method. (c) and (d) are the mapping matrices of the control runs for (c) the Neggers Model and (d) the stochastic parcel model, respectively.

The mapping matrices set a reference against which multi-parcel models can be compared. The mapping matrices A, D, E of a bulk plume models are all single numbers (or a single point in figure 4-2a). The mapping matrices of two types of multi-parcel models are shown here for comparison with the LES results. One is the model developed in Neggers *et al.* (2002) (figure 4-2c), where there is only detrainment for updrafts with the lowest q_t, and the entrainment rate increases as q_t' decreases. The mapping matrix A is a single line slightly below the 1-to-1 line. This line is further away from the 1-to-1 line at low q_t values. This feature results from the assumption in the Neggers *et al*. model that entrainment rate is inversely proportional to w, which is well correlated with q_t. Another model is the stochastic parcel model (Nie and Kuang 2012a, Romps and Kuang 2010) (Fig 2d). For the mapping matrix A, there is a strong peak on the 1-to-1 line, representing unmixed parcels. There is also a broad triangular region below, which is due to stochastic entrainment. The detrainment rate is non-zero over all q_t values and decrease as q_t increases. As is apparent from figure 4-2, the mapping matrices from the muliti-parcel models differ substantially from those deduced from the LES. A prominent difference is that because in-cloud mixing is not included in the multi-parcel models, their mapping matrices A are all zero above the 1-to-1 line. This discrepancy is also pointed out when Nie and Kuang (2012a) used their model to reproduce the updraft statistics using the tracer encoding method of Romps and Kuang 2010). Addition of this missing component should be considered for future models.

The difference of the matrices between the control runs and the perturbed runs, averaged over the 150 pairs of ensemble members, are shown in figure 4-2b. The error bars for δD and δE are standard deviation estimated by a jackknife method that leaves out one pair of runs at a time. As

expected, with the temperature perturbation, more mass flux is detrained (generally positive δD). The reason for the variations of δD with q_t is not clear and left to future study.

For δA , the pattern is a general upward shift to higher q_t' at level n+1 because the warm anomaly tends to preferentially eliminate mixtures with low q_t (less active) (Nie and Kuang 2012a). The positive δE shows more entrainment of environmental air in response to the positive temperature perturbation. A possible explanation of the enhanced entrainment is that the warm anomaly acts as a buoyancy barrier and slows down the updrafts, so that there is more time for entrainment per unit distance (Neggers *et al.* 2002), although more work is needed to test this idea. We note that this dependence, if existent, is not strong enough to explain the in-cloud heterogeneity in the way hypothesized in Neggers *et al.* (2002), and in-cloud heterogeneity is mostly caused by stochastic entrainment, as shown in Romps and Kuang (2010).

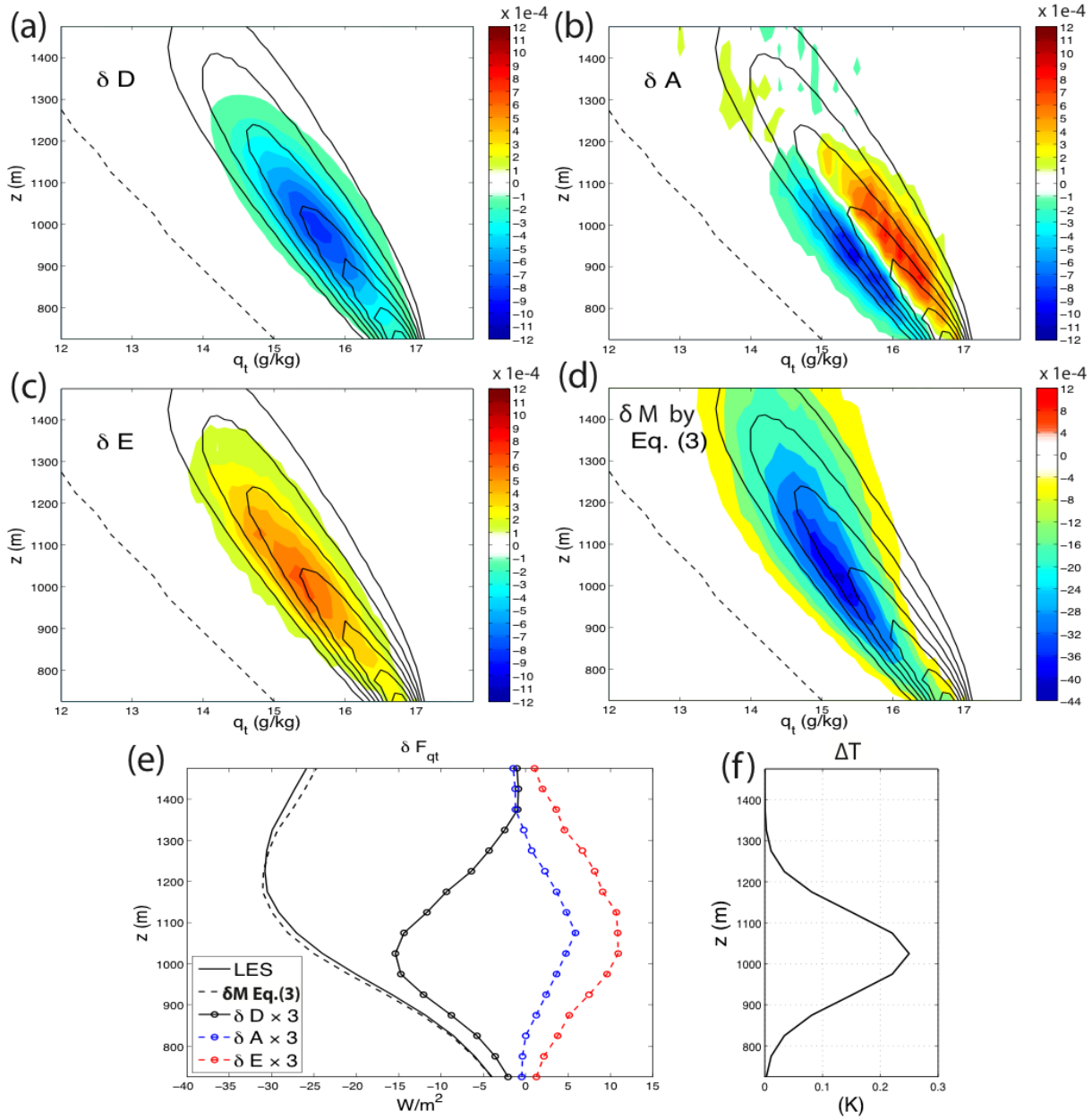

Figure 4-3: The color contours in (a)-(c) are the local sources terms in equation (4.3). The color contours in (d) is the total δm computed from equation (4.3). In (a)-(d), the color contours are in units of $kg\ m^{-2}\ s^{-1}$ per g kg^{-1} (i.e. normalized by the bin interval). (e) is the δF_{qt} corresponding to mass flux changes shown in (a)-(d), together with δF_{qt} from the LES. In (e) the δD, δA and δE terms are multiplied by a factor of 3 for better illustration. (f) introduced temperature perturbation.

The contribution of each component can be estimated using equation (4.3) for all levels. The δD, δA and δE terms in equation (4.3) are local (in z) sources to the δm_{n+1}. The inherited term, although dominating the equation, is simply the accumulated impacts from levels below. The local source terms are shown in figure 4-3a to c, together with the control run mass flux distribution (background black contour) and control environmental q_t (the far left black dashed line). The δD term is strongly negative, and contributes to the decrease of mass flux. The δE term is positive, but to a lesser extent. The δA term shows a shift from the left to the right of the ridge of the control mass flux distribution. It leads to a stronger reduction in mass flux at lower q_t and the increase of updraft mean q_t in the perturbed cases. We apply equation (4.3) recursively starting from a level slightly above cloud base (675 m height) upward with the local source terms added in each layer. The total δm computed from the chain rule (equation (4.3)), shown in figure 4-3d, is very close to the δm directly sampled from LES, a validation of the chain rule separation. In figure 4-3e, effects of these terms are summarized in terms of δF_{qt} (using equation (4.1)). It shows that the local source terms are mostly confined in the perturbed layer. Although δm is still large above the perturbed layer, it is mostly accumulated over the perturbed layers below.

4.5 Summary and Discussions

A new framework for diagnosing mixing in cumulus convection is proposed, where the vertical evolution of the cloud mass flux distribution as a function of given parcel properties is viewed as a mapping process. By analyzing the trajectories of LPDM embedded in an LES, the matrices that characterize this mapping process are constructed. The framework is applied to the shallow cumulus convection case of BOMEX. The mapping matrices of two multi-parcel models are compared with those from the LES, showing major discrepancies. Changes in the mapping matrices in response to a small temperature perturbation in the cloud layer are used to better understand such responses, yielding conclusions similar to those reached in Nie and Kuang (2012a) using a different analysis. We believe that these mapping functions provide a more complete description of the mixing process that helps to better connect LES with convective parameterization, and are a useful extension to the bulk entrainment/detrainment rates of the bulk plume model.

Although only the cloudy updrafts are considered here, the downdraft mass flux can be treated as a downward mapping in the same way. It may be necessary to account for the effects from, for example, precipitation driven downdrafts in deep convection and the subsidence shell in shallow convection (Heus and Jonker 2007, Jonker *et al.* 2008). Accounting for both the updrafts and downdrafts and the potential exchange between them in the mapping framework will be explored in future work.

CHAPTER 5

CONCLUSIONS AND FUTURE PROSPECTS

5.1 Conclusions

In this thesis, we probe the dynamics of shallow cumulus convection using LES and several other models and tools.

In Chapter 2, the responses of a shallow cumulus ensemble to large-scale temperature and moisture perturbations are investigated using an LES and a stochastic parcel model. The SPM in general reproduces the LES responses to large-scale temperature and moisture perturbations, not only in terms of the domain mean heating and moistening tendencies, but also in terms of changes in the statistics of the cloudy updrafts. The stochastic entrainment scheme in the SPM is key for the SPM to match the LES results, which suggests that the stochastic entrainment approach is a good way of representing the mixing process in simple models. A positive temperature perturbation to the environmental sounding forms a buoyancy barrier that inhibits cloudy updrafts that have lower initial θ_e or entrain heavily. For parcels that have the same amount of entrainment, the height at which parcels entrain is important in deciding their fate. Parcels entraining at higher altitudes are more likely to survive the buoyancy barrier and vice

versa. Convective heating responses to moisture perturbations above the cloud base are quite small for a shallow cumulus regime like BOMEX.

In Chapter 3, we introduce a parameterization of shallow cumulus convection (including subcloud layer turbulence) based on the stochastic parcel model. The parameterization gives promising results in terms of both the simulated mean state and the simulated responses to temperature and moisture perturbations.

In Chapter 4, a new framework for diagnosing mixing in cumulus convection is proposed, where the vertical evolution of the cloud mass flux distribution as a function of given parcel properties is viewed as a mapping process. By analyzing the trajectories of LPDM embedded in a LES, the matrices that characterize this mapping process are constructed. The framework is applied to the shallow cumulus convection case of BOMEX. The mapping matrices of two multi-parcel models are compared with those from the LES, showing major discrepancies. Changes in the mapping matrices in response to a small temperature perturbation in the cloud layer are used to better understand such responses, yielding conclusions similar to those reached in Nie and Kuang (2012a) using a different analysis. We believe that these mapping functions provide a more complete description of the mixing process that helps to better connect LES with convective parameterization, and are a useful extension to the bulk entrainment/detrainment rates of the bulk plume model.

5.2 Future prospects

With the fast advances in computer technology, numerical models are able to explicitly resolve convection in larger scales than before. Works in this direction include the development of super parameterization in GCMs (e.g. Khairoutdinov and Randall 2001), Global CRMs (e.g. Sato *et al.*

2009), and LES in continental scales. However, better simulations do not equate to a deeper understanding of convective dynamics unless efforts are made to digest the results of the simulations. In the foreseeable future, convection dynamics and convective parameterization is still a challenging but fruitful area.

While there are many directions worth exploring, several directions that are closely related to the study of this thesis are discussed here.

a) Unified convective parameterizations

In GCMs, convection in different convective regimes is often parameterized separately using different parameterization schemes. However, in the real atmosphere, the transition of convection from one regime to another is continuous and usually smooth. The separation of convective parameterizations in GCMs causes some problems with great impacts on climate. One example is the too early peak of diurnal precipitation (e.g. Yang and Slingo 2001, Dai and Trenberth 2004).

Ideally, a unified parameterization should represent different convective regimes and the transitions between them, for example, the transition from dry convective boundary layers to stratocumulus to shallow convection to deep convection. Efforts have been put in this direction (e.g. Hohenegger and Bretherton 2011, Mapes and Neal 2011), however the problem is still unsettled. Although the parameterization we proposed in Chapter 3 focuses on shallow cumulus convection, it has the potential to be further developed to cover other convective regimes. To achieve that goal, additional components should be included, for example, the downdrafts in deep convection.

b) Cold pool organization of convection

Convective downdrafts, driven by precipitation associated with convection itself, form cold pools in the planetary boundary layer. Cold pools can strengthen convection and organize scattered convection into Mesoscale Convective Systems (e.g. Houze and Betts 1981), delay the diurnal precipitation peak (e.g. Rio et al. 2009), or trigger precipitation extreme events (Del Genio and Kovari 2002). Despite the importance of the cold pool organization, it is not taken into account by most convective parameterizations in GCMs due to our poor understanding (Tao and Moncrieff 2009), leading to problems such as incorrect timing of diurnal cycle of precipitation (e.g. Rio et al. 2009), and poor simulations of the Madden–Julian oscillation (Kim et al. 2009; Benedict et al. 2013), and so on.

The goal is to better understand the cold pool organization of convection and to improve its representation in convective parameterizations. The LPDM seems to be a useful tool to help us to quantify some key processes of the cold pool organization. Related to previous prospect, the parameterization of the cold pool organization can be incorporated with the stochastic parcel parameterization.

c) Transports and reactions of chemical tracers in convection

The impact of chemical tracers (and aerosols) on climate is less well understood, and there are large uncertainties of their climate feedbacks. Convection plays a major role in transporting chemical tracers from the surface to the free troposphere, and the cloudy liquid water is essential to the aqueous phase reactions (for example the aqueous phase oxidation of sulfur dioxide). Simulating transports and reactions of chemical tracers in a CRM can provide a benchmark for the convective parameterizations of the tracers, which will further benefit the chemical transport

models and climate simulations. It can also help to study convective dynamics by providing additional information and setting extra constraints.

The effects of cloudy air inhomogeneity in the transport and reactions of chemical tracers should be evaluated. As we discussed in section 1.2.3., the bulk plume model has the flaw that entrainment and detrainment are tracer-dependent. The errors introduced by this flaw should also be assessed and corrected if it is large. The stochastic parcel model (Chapter 3) is versatile enough to include the chemical component. This parcel model and the mapping diagnostic framework in Chapter 4 seem to be useful tools in addressing these questions.

Appendix A

Sensitivity Tests of the LES

In this appendix, we explore the sensitivity of the results in Chapter 2 in Fig. 2-2 to model resolution and to the size of the protective halo around cloudy updrafts used in tracer encoding. The list of sensitivity experiments is given in Table A1 and the results are shown in figure A1.

To test the resolution dependence of the LES, in addition to the $dx = dy = dz = 25\ m$ case (the CTL run), we have made experiments with $dx = dy = 100\ m$ and $dz = 50\ m$ (the R100 run), and with $dx = dy = dz = 12.5\ m$ (the R12.5 run). In the R100 run, the w contours are oriented from upper left to lower right. In the R12.5 run, on the other hand, the w contours are more vertical in regions with high purity and more horizontal in regions with high encoded θ_e, similar to what was seen in the control experiment, indicating that such behaviors are robust for high-resolution runs. These results are also consistent with our hypothesis in Section 2.3.1 that the different behaviors in w and thermodynamic variables such as θ_e are due to intra-cloud variations; the higher-resolution simulations better resolve the clouds and therefore have more intra-cloud variations.

To further test the role of intra-cloud variations, we average the output from the control experiment, which has $dx = dy = dz = 25\ m$ to a grid of $dx = dy = 100\ m$ and $dz = 50\ m$ before computing the statistics. The results, shown in the fourth row of figure A1 and labeled as R25-b, are similar to those from the R100 run, with w and θ_e exhibiting similar behaviors. This further supports the notion that the different behaviors in w and thermodynamic variables such as θ_e are due to intra-cloud variations.

We have also tested the sensitivity to an uncertain parameter in the tracer encoding procedure.

As described in Section 2.2.1, with the tracer-encoding technique, the purity and equivalent potential temperature tracers are set to zero at every time step above the tracer release level except in the vicinity of cloudy updrafts, which is defined by a protective halo surrounding the cloudy updrafts. The size of this protective halo should be large enough to preserve tracer values at grid points that, while not qualified as cloudy updrafts themselves, are part of the circulation immediately associated with the cloudy updrafts. The size of this protective halo should also be small enough so that air not associated with the ongoing cloudy updrafts (i.e., the environmental air) has zero tracer values. The precise value of the halo size is uncertain, which is a limitation of the tracer-encoding technique. For the control experiments presented in figure 2-2a to c, the halo size is three grid points (or 75 m). In experiment R25-c, we set the halo size to 300 m. The main effect is a small shift in the mass flux distribution to- ward higher purity as expected from the wider protective halo. The salient features of the w distribution remain unchanged.

TABLE A1. Summary of the numerical experiments used in the sensitivity tests.

Simulation	Resolution (m, dx * dy * dz)	Tracer-protecting halo size (m)	Remarks
R100	100 * 100 * 50	300	
R25-a(CTL)	25 * 25 * 25	75	Control run
R12.5	12.5 * 12.5 * 12.5	75	
R25-b	25 * 25 * 25	75	Coarsened resolution for sampling
R25-c	25 * 25 * 25	300	

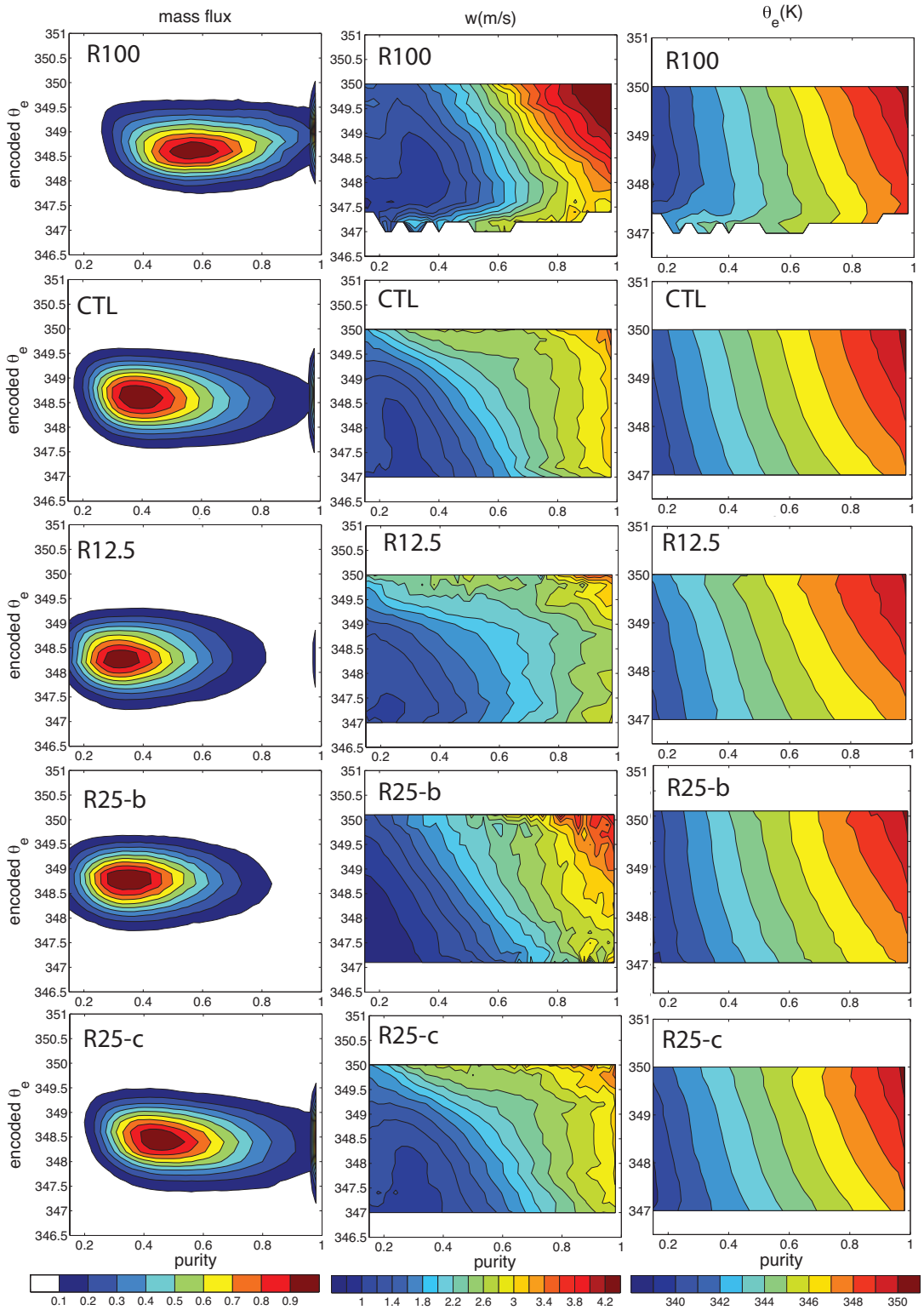

Figure A1: Cloud updraft statistics of (left) mass flux, (middle) w, and (right) θ_e with different LES settings as listed in Table A1. The simulation names are labeled on the top-left corner of

Figure A1 (continued): each panel. The panels for the CTL simulations are as in figure 2-2a to c and are included here to facilitate comparison.

References

Arakawa, A., and W. H. Schubert, 1974: Interaction of a cumulus cloud ensemble with the large-scale environment. Part I, *J. Atmos. Sci*., **31**, 674–701.

Austin, P. H., M. B. Baker, A. M. Blyth, and J. B. Jensen, 1985: Small-scale variability in warm continental cumulus clouds. *J. Atmos. Sci.,* **42,** 1123–1138.

Bechtold, P., E. Bazile, F. Guichard, P. Mascart, and E. Richard, 2001: A mass-flux convection scheme for regional and global models. *Quart. J. Roy. Meteor. Soc.*, **127**, 869 –886.

Benedict, J. J., E. D. Maloney, A. H. Sobel, D. M. Frierson, L. J. Donner, 2013: Tropical Intraseasonal Variability in Version 3 of the GFDL Atmosphere Model. *J. Climate*, **26**, 426–449.

Betts, A. K., 1975: Parametric Interpretation of Trade-Wind Cumulus Budget Studies. *J. Atmos. Sci.*, **32**, 1934–1945.

Betts A. K. 1982: Saturation point analysis of moist convective overturning. *J. Atmos. Sci.*, **39**, 1484–1505.

Blyth, A. M., 1993: Entrainment in cumulus clouds. *J. Appl. Meteor.*, **32**, pp. 626–641.

Böing, Steven J., Harm J. J. Jonker, A. Pier Siebesma, Wojciech W. Grabowski, 2012: Influence of the Subcloud Layer on the Development of a Deep Convective Ensemble. *J. Atmos. Sci.*, **69**, 2682–2698.

Bony, S. and J.-L. Dufresne, 2005: Marine boundary layer clouds at the heart of tropical cloud feedback uncertainties in climate models. Geophys. Res. Lett, **32**, doi:10.1029/2005GL023 851.

Bony, S., J.-L. Dufresne, H. L. Treut, J.-J. Morcrette, and C. Senior, 2004: On dynamic and thermodynamic components of cloud changes. *Climate Dyn.*, **22**, 71–86.

Bretherton, C. S., J. R. McCaa, and H. Grenier, 2004: A new parameterization for shallow cumulus convection and its application to marine subtropical cloud-topped boundary layers. Part I: Description and 1D results, *Mon. Wea. Rev.*, **132**, 864–882.

Cheinet, S., 2003: A multiple mass-flux parameterization for the surface-generated convec- tion. a multiple mass-flux parameterization for the surface-generated convection. part i: Dry plumes. *J. Atmos. Sci*., **60**, 2313–2327.

Cheinet, S., 2004: A multiple mass flux parameterization for the surface-generated con- vection. Part II: Cloudy Cores, *J. Atmos. Sci*., **61**, 1093–1113.

Dawe, J. T., and P. H. Austin, 2011a: Interpolation of LES Cloud Surfaces for Use in Direct Calculations of Entrainment and Detrainment, *Mon. Wea. Rev.*, **139**, 444–456.

Dawe, J. T., and P. H. Austin, 2011b: The Influence of the Cloud Shell on Tracer Budget Measurements of LES Cloud Entrainment, *J. Atmos. Sci*., **68**, 2909–2920.

Del Genio A.D. and W. Kovari, 2002: Climatic properties of tropical precipitating convection under varying environmental conditions. *J. Clim*., **15**, 2597-2615.

Dufresne, J.-L., S. Bony, 2008: An Assessment of the Primary Sources of Spread of Global Warming Estimates from Coupled Atmosphere–Ocean Models. *J. Climate*, **21**, 5135–5144.

Durran, D. R., 1999: Numerical methods for wave equations in geophysical fluid dynamics. Springer, 267 pp.

Emanuel, K. A., 1991: A scheme for representing cumulus convection in large-scale models, *J. Atmos. Sci.*, **48**, 2313–2329.

Golaz, J.-C., V. E. Larson, and W. R. Cotton, 2002: A pdf-based model for boundary layer clouds. part i: Method and model description. *J. Atmos. Sci*., **59**, 3540–3551.

Gustafson Jr., W.I., L.K. Berg, R.C. Easter, S.J. Ghan, 2008: The Explicit-Cloud Parameterized-

Pollutant hybrid approach for aerosol-cloud interactions in multiscale modeling framework models: tracer transport results. *Environ Res Lett*., **3**, 1–7.

Hack, J. J., 1994: Parameterization of moist convection in the National Center for Atmospheric Research community climate model (CCM2), *J. Geophys. Res*., **99(D3)**, 5551–5568.

Heus, T., and H. J. J. Jonker, 2007: Subsiding Shells around Shallow Cumulus Clouds, *J. Atmos. Sci.*, **65**, 1003–1018.

Heus, T., G. van Dijk, H. J. J. Jonker, and H. E. A. van den Akker, 2008: Mixing in shallow cumulus clouds studied by Lagrangian particle tracking, *J. Atmos. Sci*., **65**, 2581–2597.

Heus, T., H. J. J. Jonker, H. E. A. Van den Akker, E. J. Griffith, M. Koutek, and F. H. Post (2009), A statistical approach to the life cycle analysis of cumulus clouds selected in a virtual reality environment, *J. Geophys. Res*., **114**, D06208.

Herman M. J., and Z. Kuang, 2013: Linear response functions of two convective parameterization schemes, *J. Advances in Modeling Earth Systems*, submitted.

Hohenegger, C. and Bretherton, C. S.: Simulating deep convection with a shallow convection scheme, Atmos. Chem. Phys., 11, 10389-10406, doi:10.5194/acp-11-10389-2011, 2011.

Holland, J. Z., and E. M. Rasmusson, 1973: Measurement of atmospheric mass, energy, and momentum budgets over a 500-kilometer square of tropical ocean., *Mon. Wea. Rev*., **101**, 44–55.

Houze, R. A., 1993: Cloud Dynamics, Volume 53, Academic Press, 239-245 pp.

Houze R.A. Jr. and A.K. Betts, 1981: Convection in GATE. Rev. *Geophys. Space Phys*., **19**. 541-576.

Wyngaard, J. C. and C.-H. Moeng, 1992: parameterizing turbulent diffusion through the joint probality density. *Boundary-layer meteorology*, **60**, 1-13.

Jonker, H. J. J., T. Heus, and P. P. Sullivan, 2008: A refined view of vertical mass transport by cumulus convection, *Geophys. Res. Letts*., **35**, L07810, doi:10.1029/2007GL032606.

Kain, J. S. and M. Fritsch, 1990: A one-dimensional entraining/detraining plume model and its application in convective parameterization. *J. Atmos. Sci*., **47**, 2784 –2802.

Khairoutdinov, M. F., and D. A. Randall (2001), A cloud-resolving model as a cloud parameterization in the NCAR Community Climate System Model: Preliminary results, Geophys. Res. Lett., 28, 3617–3620.

Kim D., et al., 2009: Application of MJO simulation diagnostics to climate models. *J. Climate*, **22**, 6413–6436.

Krueger, S. K., C.-W. Su, and P. A. Mcmurtry, 1997: Modeling entrainment and finescale mixing in cumulus clouds. *J. Atmos. Sci*., **54**, 2697–2712.

Kuang, Z., and C. S. Bretherton, 2006: A Mass-Flux Scheme View of a High-Resolution Simulation of a Transition from Shallow to Deep cumulus convection, *J. Atmos. Sci.*, **63**, 1895–1909.

Kuang, Z., 2010: Linear response functions of a cumulus ensemble to temperature and moisture perturbations and implication to the dynamics of convectively coupled waves, *J. Atmos. Sci.*, **67**, 941–962.

Kuang, Z., 2011: The wavelength dependence of the gross moist stability and the scale selection in the instability of column integrated moist static energy, *J. Atmos. Sci*., **68**, 61-74.

Kuang, Z., 2012: Weakly forced mock-Walker cells, *J. Atmos. Sci*., **69**, 2759-2786.

Lamontagne, R. G. and J. W. Telford, 1983: Cloud-top mixing in small cumuli. *J. Atmos. Sci.* **40**, 2148–2156.

Lappen, C.-L. and D. A. Randall, 2001: Toward a unified parameterization of the boundary layer

and moist convection. part i: A new type of mass-flux model. *J. Atmos. Sci*., **58**, 2021–2036.

Larson, V. E., J.-C. Golaz, and W. R. Cotton, 2002: Small-scale and mesoscale variability in cloudy boundary layers: Joint probability density functions. *J. Atmos. Sci*., **59**, 3519– 3539.

Li, Q., D. J. Jacob, T. D. Fairlie, H. Liu, R. V. Martin, and R. M. Yantosca, 2002: Stratospheric versus pollution influences on ozone at Bermuda: Reconciling past analyses, *J. Geophys. Res.*, **107(D22)**, 4611.

Lin, C., and A. Arakawa, 1997: The Macroscopic Entrainment Processes of Simulated Cumulus Ensemble. Part II: Testing the Entraining-Plume Model. *J. Atmos. Sci.*, **54**, 1044–1053.

Lu, C., Y. Liu, S. Niu, and A. M. Vogelmann, 2012: Lateral entrainment rate in shallow cumuli: Dependence on dry air sources and probability density functions, Geophys. Res. Lett., **39**, L20812.

Lu, J., G. A. Vecchi, and T. Reichler, 2007: Expansion of the Hadley cell under global warming, *Geophys. Res. Lett*., **34**, L06805, doi:10.1029/ 2006GL028443.

Malkus, J. S., and R. S. Scorer, 1955: The erosion of cumulus towers. *J. Meteor.*, **12**, 43–57.

Mapes, B. E., 2004: Sensitivities of cumulus-ensemble rainfall in a cloud-resolving model with parameterized large-scale dynamics. *J. Atmos. Sci*., **61**, 2308–2317.

Mapes, B. E., and R. Neale, 2011: Parameterizing convective organization to escape the entrainment dilemma. *J. Adv. Model. Earth Syst.,* **3,** M06004.

Moore, M., and Z. Kuang, P. N. Blossey, 2013: Clarifying the amount effect, *Geophys. Res. Letts.,* in prep,

Morton, B. R., G. I. Taylor, and J. S. Turner, 1956. Turbulent gravitational convection from maintained and instantaneous sources. *Proc. R. Soc. London A*, **234**, 1–23.

Neggers, R. A. J., A. P. Siebesma, and H. J. J. Jonker, 2002: A multiparcel model for shallow cumulus convection., *J. Atmos. Sci*., **59**, 1655–1668.

Neggers, R. A., J. D. Neelin, and B. Stevens, 2007: Impact mechanisms of shallow cumulus convection on tropical climate dynamics. *J. Climate*, **20,** 2623–2642.

Nie, J., and Z. Kuang, 2012a: Responses of Shallow Cumulus Convection to Large-scale Temperature and Moisture Perturbations: a comparison of Large-eddy simulations and a convective parameterization based on stochastically entraining parcels, *J. Atmos. Sci*, **69**, 1936–1956.

Nie, J. and Z. Kuang, 2012b: Beyond bulk entrainment and detrainment rates: A new framework for diagnosing mixing in cumulus convection, *Geophys. Res. Lett.,* **39**, L21803, doi:10.1029/2012GL053992.

Ooyama, K. V., 1971: A theory on parameterization of cumulus convection. *J. Meteor. Sci*., **49**, 755-756.

Paluch, I. R., 1979: The entrainment mechanism in Colorado cumili. *J. Atmos. Sci.* **36**, 2467–2478.

Pincus, R., H. W. Barker, and J. J. Morcrette, 2003: A fast, flexible, approximate technique for computing radiative transfer in inhomogeneous cloud fields. *J. Geophys. Res*., **108**, doi:10.1029/2002JD003 322.

Plant, R. S.: A review of the theoretical basis for bulk mass flux convective parameterization, *Atmos. Chem. Phys.*, **10**, 3529-3544, doi:10.5194/acp-10-3529-2010, 2010.

Randall, D. A.,, J. A. Coakley, C. W. Fairall, R. A. Knopfli, and D. H. Lenschow, 1984: Outlook for research on marine subtropical stratocumulus clouds. *Bull. Amer. Meteor. Soc*., **65**, 1290– 1301.

Raymond, D. J. and A. M. Blyth, 1986: A stochastic mixing model for nonprecipitating cumulus clouds. *J. Atmos. Sci*., **43**, 2708–2718.

Raymond, D. J. and M. J. Herman, 2011: Convective quasi-equilibrium reconsidered. *J. Adv. Model. Earth Syst*., **3**, M08003, doi:10.1029/2011MS000079.

Rieck, Malte, Louise Nuijens, Bjorn Stevens, 2012: Marine Boundary Layer Cloud Feedbacks in a Constant Relative Humidity Atmosphere. *J. Atmos. Sci.*, **69**, 2538–2550.

Rio, C., F. Hourdin, J.-Y. Grandpeix, and J.-P. Lafore (2009), Shifting the diurnal cycle of parameterized deep convection over land, Geophys. Res. Lett., 36, L07809.

Romps, D. M., 2008: The dry-entropy budget of a moist atmosphere. *J. Atmos. Sci*., **65**, 3779–3799.

Romps, D. M., 2010: A Direct Measure of Entrainment, *J. Atmos. Sci*., **67**, 1908–1927.

Romps, D. M., and Z. Kuang (2010), Nature versus Nurture in Shallow Convection, *J. Atmos. Sci*., **67**, 1655–1666.

Sato, T., H. Miura, M. Satoh, Y. N. Takayabu, Y. Wang, 2009: Diurnal Cycle of Precipitation in the Tropics Simulated in a Global Cloud-Resolving Model. *J. Climate*, **22**, 4809–4826.

Sherwood, S., M. Colin, and F. Robinson, 2010: A revised conceptual model of cumulus clouds as thermal vortices. Eos, Trans. Amer. Geophys. Union, (Fall Meeting Suppl.) abstract A24C-04.

Siebesma, A. P., and J. W. M. Cuijpers, 1995: Evaluation of parametric assumptions for shallow cumulus convection, *J. Atmos. Sci*., **52**, 650–666.

Siebesma, A. P., and Coauthors, 2003: A Large Eddy Simulation Intercomparison Study of Shallow Cumulus Convection, *J. Atmos. Sci*., **60**, 1201–1219.

Slingo, A., 1990: Sensitivity of the Earth's radiation budget to changes in low clouds. *Nature*,

343, 49–51.

Soden, B. J., and G. A. Vecchi, 2011: The vertical distribution of cloud feedback in coupled ocean-atmosphere models, *Geophys. Res. Lett*., **38**, L12704.

Squires, P., 1958: The microstructure and colloidal stability of warm clouds. Part I. The relation between structure and stability. *Tellus* **10**, 256 – 261.

Squires, P., and J. S. Turner, 1962: An entraining jet model for cumulo-nimbus updraughts. *Tellus*, **16**, 422–434.

Stohl, A., and P. James, 2005: A Lagrangian Analysis of the Atmospheric Branch of the Global Water Cycle. Part II: Moisture Transports between Earth's Ocean Basins and River Catchments. *J. Hydrometeor*, **6**, 961–984.

Stommel, H., 1947: Entrainment of air into a cumulus cloud. *J. Meteorol.* **4**, 91–94.

Stull, R. B., 1988: An Introduction to Boundary Layer Meteorology. Kluwer Academic, 670 pp.

Sušelj, Kay, J. Teixeira, G. Matheou, 2012: Eddy Diffusivity/Mass Flux and Shallow Cumulus Boundary Layer: An Updraft PDF Multiple Mass Flux Scheme. *J. Atmos. Sci.*, **69**, 1513–1533.

Sušelj, K., J. Teixeira, D. Chung, 2013: A Unified Model for Moist Convective Boundary Layers Based on a Stochastic Eddy-Diffusivity/Mass-Flux Parameterization. *J. Atmos. Sci*, **70**, 1929-1953.

Taylor, G. R. and M. B. Baker, 1991: Entrainment and detrainment in cumulus clouds. *J. Atmos. Sci.* **48**, 112–121.

Tiedtke, M., 1989: A comprehensive mass flux scheme for cumulus parameterization in large-scale models. *Mon. Wea. Rev*., **117**, 1779–1800.

Tulich, S. N, and B. E. Mapes, 2010: Transient Environmental Sensitivities of Explicitly

Simulated Tropical Convection, *J. Atmos. Sci*., **67**, 923–940.

Vecchi, G. A., and B. J. Soden, 2007: Increased tropical Atlantic wind shear in model projections of global warming, *Geophys. Res. Lett*., **34**, L08702.doi:10.1029/2006GL028905.

Warner, J., 1955: The water content of cumuliform clouds. *Tellus* **7**, 449 – 457.

Warner, J., 1970: On Steady-State One-Dimensional Models of Cumulus Convection. *J. Atmos. Sci.*, **27**, 1035–1040.

Warren, F. W. G., 1960: Wave resistance to vertical motion in a stratified fluid. *J. Fluid Mechanics,* **7**, 209–229.

Yanai, M., S. Esbensen, and J.-H. Chu, 1973: Determination of bulk properties of tropical cloud clusters from large-scale heat and moisture budgets. *J. Atmos. Sci*., **30**, 611– 627.

Yang, G., J. Slingo, 2001: The Diurnal Cycle in the Tropics. *Mon. Wea. Rev.*, **129**, 784–801.

Yano, J.-I., E. Machulskaya, P. Bechtold, R. S. Plant, 2013: Bells and Whistles of Convection Parameterization. *Bull. Amer. Meteor. Soc.*, **94**, ES5–ES7.

Yeo, K, and D. M. Romps, 2012: Measurement of convective entrainment using Lagrangian particles, *J. Atmos. Sci*., **70**, 266–277.

Weil, J. C., P. P. Sullivan, and C. H. Moeng, 2004: The use of large-eddy simulation in lagrangian particle dispersion models, *J. Atmos. Sci*., **61**, 2877–2887.

Wood, R., 2012: Stratocumulus Clouds. *Mon. Wea. Rev.*, **140**, 2373–2423.

Zelinka, Mark D., Stephen A. Klein, Karl E. Taylor, Timothy Andrews, Mark J. Webb, Jonathan M. Gregory, Piers M. Forster, 2013: Contributions of Different Cloud Types to Feedbacks and Rapid Adjustments in CMIP5. *J. Climate*, **26**, 5007–5027.